Journal of Photochemistry & Photobiology, A: Chemistry 450 (2024) 115433

Contents lists available at ScienceDirect

Journal of Photochemistry & Photobiology, A: Chemistry

journal homepage: www.elsevier.com/locate/jphotochem

Enhanced photocatalytic activity and stability of WO_3-AgCl/Ag composites: Surface modulation by structure-directing agents for effective sunlight treatment of pharmaceutical wastewater

Priscila Hasse Palharim [a,*], Maria Clara D'Amaro Caira [a], Carolina Gusmão [a], Bruno Ramos [b], Alan Gomes da Câmara [c], Jose Geraldo A. Pacheco [c], Orlando Rodrigues Jr. [d], Antonio Carlos Silva Costa Teixeira [a,*]

[a] Research Group in Advanced Oxidation Processes (AdOx), Department of Chemical Engineering, Escola Politécnica, University of São Paulo, São Paulo, Brazil
[b] Microfluidic and Photoelectrocatalytic Engineering Lab (μFEC), Department of Chemical Engineering, FEI University Center, São Bernardo do Campo, Brazil
[c] Laboratory of Refining and Cleaner Technology, Department of Chemical Engineering, Center of Technology and Geosciences, Institute for Petroleum and Energy Research, Federal University of Pernambuco, Recife, Brazil
[d] Nuclear and Energy Research Institute, IPEN/CNEN, Av. Prof. Lineu Prestes, São Paulo, Brazil

ARTICLE INFO

Keywords:
Acetaminophen
Continuous reactor
Pharmaceutical effluent
Photocatalyst
Simulated sunlight

ABSTRACT

In this work, different structure-directing agents (citric acid, oxalic acid, urea, polyethylene glycol and Triton X-100) were used to synthesize WO_3-AgCl photocatalysts by a simple one-step hydrothermal method. The successful synthesis of the materials was proved through various characterization techniques (XRD, BET, SEM, TEM, EDS, UV–vis DRS, XPS, EPR, Mott-Schottky and photoluminescence). The directing agent strongly influenced the morphology of the catalysts, with the material synthesized with citric acid showing the most homogeneous distribution of WO_3 and AgCl particles, and the highest photocatalytic activity (100.0% acetaminophen removal after 30 min; $k = 0.212\ min^{-1}$). Stability tests resulted in a performance reduction of only 18.8% after four cycle times. Degradation in real effluent from a pharmaceutical industrial facility showed 83.6% acetaminophen removal. In addition, experiments in a continuous microstructured packed bed reactor revealed 97.9% steady-state contaminant removal.

1. Introduction

Tungsten trioxide (WO_3) is an *n*-type semiconductor, which has attracted increased interest due to its attractive properties in various domains, such as electrochromism, photochromism, and photocatalysis [1]. In particular, several studies have been developed over the last years on the application of WO_3 as a photocatalyst, due to its relatively narrow band gap energy (E_g) (~2.5–2.8 eV) [1,2]. However, the high recombination rate of photogenerated carriers in pure WO_3 drastically impairs its photocatalytic activity. Alternatives to circumvent this problem involve the modification of the semiconductor with metals, and combinations with other semiconductors to form heterojunctions [3,4]. In this direction, Ag nanoparticles and silver-based materials have emerged as potential candidates for improving photocatalytic efficiency and light absorption in the visible region, which represents the majority (~51%) of the available energy of the sunlight spectrum that reaches the Earth's surface [3,5]. The significantly large atomic absorption cross-section of noble metals ($\sigma = 10^{-13}$ to $10^{-12}\ cm^2$), enable them to absorb light nearly 10^4 to 10^5 times more than conventional metals ($\sigma = 10^{-17}$ to $10^{-16}\ cm^2$), which can be used for enhancing photocatalysis [6]. Among the various silver-based materials, AgCl stands out for its superior response to visible light. However, due to its strong photosensitivity, Ag^+ is continuously reduced to metallic Ag^0 when exposed to light, jeopardizing the lifetime and stability of AgCl as a photocatalyst [7]. Thus, the construction of heterojunctions with other semiconductors, such as WO_3, is one of many methods proposed to synthesize catalysts with greater stability and photocatalytic activity.

WO_3 has been synthesized using a variety of routes, such as sol–gel [8], chemical vapor deposition [9], hydrothermal [4,10,11], and anodization [12]. Among these, the hydrothermal method offers numerous advantages, particularly its ability to precisely control the morphology, crystallinity, and size of the synthesized materials [8]. In

* Corresponding authors.
E-mail addresses: pri.palharim@gmail.com (P.H. Palharim), acscteix@usp.br (A.C.S.C. Teixeira).

https://doi.org/10.1016/j.jphotochem.2023.115433
Received 4 August 2023; Received in revised form 8 December 2023; Accepted 21 December 2023
Available online 26 December 2023
1010-6030/© 2023 Elsevier B.V. All rights reserved.

this method, it is possible to control these structural parameters using *structure-directing agents* (SDAs), additives which adsorb on specific facet surfaces of the crystal during its growth stages [2,13–16]. Thus, SDAs can dynamically modify the structure of nanoparticles by inhibiting or promoting crystal growth in a way that satisfies surface energy requirements [15]. Biswas et al. [15], for example, synthesized WO_3 with various morphologies by the hydrothermal method using oxalic, citric, and tartaric acids. The authors showed that the photocatalytic performance of the oxide was significantly affected as a consequence. Sánchez Martínez et al. [17] obtained WO_3 by precipitation in the presence of urea and concluded that this reactant slows down the crystallization step in the precipitation process. Polyethylene glycol, ethylenediaminetetraacetic acid, polyvinylpyrrolidone, and polyvinyl alcohol were used in the synthesis of silver nanoparticles through a simple chemical reduction route by Ajitha and coworkers [18], who obtained particles of different sizes varying according to the structure-directing agent. Another SDA, Triton X-100, was employed in the synthesis of $BiVO_4$, playing a crucial role in the development of a cuboid-like morphology [19]. Usually, the use of SDAs and the evaluation of their effects are carried out for pure materials, and thus their effects in heterojunction or composite materials are still not well understood. Indeed, to our knowledge, no reported study has investigated the enhanced photocatalytic properties of WO_3-AgCl materials by combining the use of SDAs in the one-step hydrothermal synthesis route; nor compared the effect of different SDAs on the optical, crystalline and morphological properties of these composite materials.

In this study, five different SDAs – citric acid, oxalic acid, urea, polyethylene glycol, and Triton X-100 – were used in the synthesis of WO_3-AgCl photocatalysts. The synthesized materials were characterized using various techniques to carry out an in-depth investigation of the role these agents play in the final properties of the materials. Special focus was given to the activity of the photocatalysts under simulated solar irradiation, which was evaluated by the oxidation of a model pharmaceutical contaminant, acetaminophen (ACT). The selection of this compound is based on the concern that the inappropriate disposal of pharmaceuticals has gained in recent years, becoming a relevant environmental issue [20,21]. In order to elucidate the reactivity mechanism, EPR spectra analyses were performed to identify the radicals present in the irradiated samples. Finally, the material that showed the best photocatalytic activity in ultrapure water containing ACT was further evaluated using an effluent from a pharmaceutical industry to assess its performance in a more realistic scenario. Additional experiments were also carried out using a continuous micro packed-bed reactor to evaluate the feasibility of using the synthesized photocatalyst in continuous flow operation.

2. Materials and Methods

2.1. Materials

Acetaminophen ($C_8H_9NO_2$, CAS 103–90-2, HPLC standard, $\geq$ 99%), sodium tungstate dihydrate ($Na_2WO_4{\cdot}2H_2O$, ACS, $\geq$ 99%), silver nitrate ($AgNO_3$, ACS, PA) and DMPO (5,5-dimethyl-1-pyrroline N-oxide) were acquired from Sigma-Aldrich. Concentrated hydrochloric acid (36–38% HCl), ethanol, sodium sulfate, citric acid, oxalic acid, urea, PEG 2000, Triton X-100, formic acid, *tert*-butanol (TBA), 1,4-hydroquinone, potassium iodine (KI) and sodium azide were of analytical grade. All reactants were used without a further purification step. Ultrapure water (18.2 MΩ) from a Milli-Q® system was used to prepare all solutions.

2.2. Synthesis of photocatalysts

The one-step hydrothermal method was used to synthesize all photocatalysts [4,22]. First, 15 mL of an aqueous solution of 0.3 mol L^{-1} $Na_2WO_4{\cdot}2H_2O$ were prepared. Then, a structure-directing agent (SDA), citric acid, oxalic acid, urea, PEG 2000 or Triton X-100, was added to the solution in a 1:1 molar ratio of WO_3:SDA, except for Triton X-100 (WO_3:Triton = 30:1) and for PEG 2000 (WO_3:PEG = 20:1). Since the critical micelle concentration (CMC) of Triton surfactant in pure water is 1 mmol L^{-1}, the concentration of this SDA was selected to be 10 CMC [23]; while that of PEG was based on the literature [24]. Subsequently, $AgNO_3$ ($\geq$ 99%) was added to the solution to achieve WO_3-5% Ag (w/w). The pH was adjusted using HCl (36–38%) to reach pH 1.5. Finally, this solution was transferred to a 220-mL PTFE-lined autoclave, which was kept in an oven heated at 10 °C min^{-1} to 120 °C, and kept at this temperature for 12 h, as determined by the best conditions in our previous work [22]. The solid obtained was washed by resuspension and centrifuging three times with ethanol and once with water to eliminate any possible ionic residues. The final dispersion was dried at 80 °C for 24 h and the resulting solid was finely ground with mortar and pestle before storage and use. Exceptionally, the catalyst synthesized with urea was subsequently calcined at 500 °C for 3 h to eliminate any residual urea [17].

2.3. Characterization techniques

The morphology of the synthesized materials was investigated by scanning (SEM, Vega 3 LMU Tescan) and transmission (TEM, HRTEM; JEM-2100, Jeol Inc.) electron microscopy. The SEM analyses were carried out at 5 and 20 kV using a sample suspended in isopropanol, dripped onto a silicon substrate and dried. For the TEM analysis, the suspension was dripped onto a carbon-coated copper grid, and the equipment operated at 200 kV. The elemental composition of the synthesized materials was mapped using energy dispersive X-ray spectroscopy (EDS, STEM-EDS) coupled to the SEM equipment. The phase composition of the catalysts was investigated by powder X-ray diffraction in a D8 Focus Bruker AXS system with a Cu K-radiation source and Ni filter operating at 20 kV and 40 mA. The surface states were further surveyed by X-ray photoelectron spectrometry (XPS), using a Thermo Scientific K-Alpha photoelectron spectrometer, operating with an X-ray source (Al K_α) and a pressure of 1×10^{-8} mBar. The total surface area was evaluated by N_2 adsorption with a Gemini III 2375 apparatus (Micromeritics Instrument Corp.). The photoelectrochemical properties of the materials were investigated by (i) UV–vis diffuse reflectance spectroscopy (UV–vis DRS) using a Shimadzu 2550 spectrophotometer with an integrating sphere; (ii) steady-state photoluminescence spectroscopy (PL), performed at room temperature in a Horiba Yvon-Jobin Fluoromax-222 (Em/Exc; slit 1.0 nm) in the 350–700 nm region equipped with a Xenon lamp and a Peltier-cooled FL-123450 PMT detector; (iii) time-resolved photoluminescence measurements, conducted in a home-built single photon counting apparatus as described by Walfort et al. [25] using a 355 nm ns-pulsed laser (MPL-F-355 nm-100 mW, CNI Laser, 10 kHz) as excitation source, a photomultiplier tube (PicoQuant, PMA 192-C) as detector, and a quTAG MC (quTools) as a multichannel scaler for time-correlated single photon counting; and, lastly, (iv) Mott-Schottky measurements, which were performed in a Bio-Logic SP-200 electrochemical workstation with a three-electrode cell at room temperature. For the latter analysis, 5 mg of the photocatalyst were mixed with 100 μL of water and 100 μL of ethanol, sonicated and then ~20 μL of this slurry was drop-cast onto FTO substrates of approximately 1 cm^2, acting as a working electrode; the counter electrode was Pt wire and the reference electrode was an Ag/AgCl electrode (in saturated KCl). The experiments were carried out in the dark using a solution of 0.5 mol L^{-1} Na_2SO_4, in the potential range from −1.0 to 1.0 V (vs. Ag/AgCl), at a frequency ranging from 5 to 10 kHz. Finally, the presence of radical oxygen species generated upon photoexcitation of the materials was evaluated by electron paramagnetic resonance spectroscopy (EPR) in a Bruker EMXplus operating in the X-band at room temperature.

2.4. Photocatalytic activity assays

The photocatalytic activity of the synthesized materials was evaluated using acetaminophen (ACT) as a model pollutant. In a 25-mL reaction vessel, 10 mg of the catalyst were suspended in 10 mL of a 5-mg L^{-1} ACT solution ($pH_0 \sim 5.6$, not adjusted). The reaction temperature was maintained at 21 °C using a cooling bath. The suspension was stirred in the dark for 30 min to reach adsorption–desorption equilibrium, and then exposed to UV–Vis irradiation, provided by a high-power metal halide lamp (400 W HPI-T, Phillips Co.) mounted on a parabolic reflector and positioned 15 cm from the solution surface (irradiated surface of 9.1 cm^2). The experiments were carried out for 120 min, over which 200-μL samples were collected, diluted five times, filtered, and submitted for HPLC analysis. The schematic diagram and the emission spectrum of the lamp are shown in Fig. S1. A spectroradiometer (Luzchem, SPR-4002) was used to measure the UV-A irradiance (300–400 nm) on the surface of the solution, set to ~4.6 mW cm^{-2}, the equivalent output of the standard AM 1.5G solar spectrum at sea level [5]. ACT concentration was measured using a Shimadzu LC20 HPLC chromatograph equipped with a C18 column (Prominent) and a UV–vis detector (SPD20A). The mobile phase was methanol:water (25:75), with a flow rate of 1.0 mL min^{-1}, injection volume of 50 μL, and oven temperature at 35 °C. The retention time was about 7 min, and the detection wavelength was 243 nm. The limit of detection for ACT was 0.08 mg L^{-1}, and the limit of quantification was 0.24 mg L^{-1}.

3. Results

3.1. Phase structure

The XRD diffractograms in Fig. 1 show well-defined peaks, evidencing high crystallinity and indicating that the addition of structure-directing agents (SDAs) does not promote phase changes. The XRD patterns of the pure WO_3, synthesized without any silver precursor or SDA, as well as the materials synthesized with various SDAs, correspond well to JCPDS Card No. 00–033-1387 of the hexagonal WO_3. In addition to it, the patterns of the WO_3-AgCl materials include the cubic phase of AgCl, according to JCPDS Card No 96–901-1667. For materials produced without SDAs or with Triton X-100, an additional peak is observed at $2\theta = 16.3°$, which corresponds to the orthorhombic structure $W_8Ag_{16}O_{32}$ (JCPDS Card No. 96–150-9985). No peaks related to metallic silver were found, which is attributed to its low content.

In general, the particles grew preferentially in the directions of the

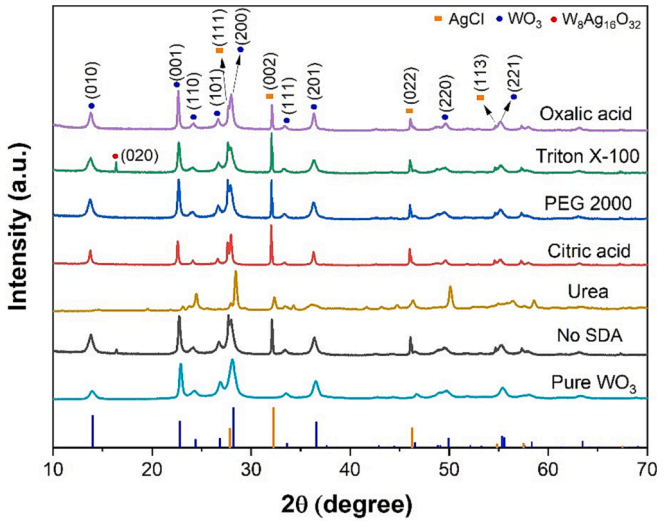

Fig. 1. XRD patterns for the pure materials and photocatalysts synthesized using different structure-directing agents.

WO_3 planes (010), (001), (200) and (201) and of the AgCl (111), (002) and (022) facets. When urea was added to the synthesis, only the planes (110), (200) and (220) of the WO_3 structure and (002) and (022) of the AgCl structure were clearly defined, indicating that this SDA particularly inhibited the formation of AgCl. The peak at $2\theta = 32.3°$, referring to the crystal plane (002) of AgCl, was also observed at high intensities for catalysts synthesized in the presence of Triton X-100, PEG 2000 and citric acid. Furthermore, the peak at $2\theta = 27.8°$, associated with the crystalline plane (111) of AgCl which partially overlaps the plane (200) of WO_3, shows better separation from the latter in the material prepared using citric acid.

The lattice parameters calculated by the Rietveld method [26] and the crystallite size obtained by the Scherrer equation, using XRD data, are shown in Table 1. The lattice parameters values were quite similar to those of the hexagonal structure of WO_3 according to JCPDS Card No. 00–033-1387 ($a = b = 7.30$ Å and $c = 3.90$ Å), with expected variations due to the presence of AgCl. Exceptionally, the lattice parameters of the catalyst synthesized in the presence of urea were slightly smaller, which may be related to the calcination step [27]. The average AgCl crystallite size (Table 1) increased for all the materials obtained in the presence of SDAs, especially those with Triton X-100 and PEG 2000. On the other hand, the mean WO_3 crystallite sizes in the material prepared without SDAs and those synthesized with Triton X-100 and PEG 2000 were remarkably similar, while the samples synthesized in the presence of citric and oxalic acids exhibited larger crystallites.

3.2. Morphology

SEM images of synthesized photocatalysts in the absence and presence of different SDAs, shown in Fig. 2 and Fig S2, indicate that the presence of the agents strongly affect the morphology of the materials. The average particle size was estimated from the micrographs by measuring the diameter (or its equivalent for a non-spherical particle) of a number of particles ($n \sim 50$) using an image processing software (ImageJ). The material prepared without additives (Fig. S2) consisted of cube-like to nearly spherical AgCl, with average size (d_{avg}) of 3.9 ± 1.6 μm, coupled to an agglomerate of thin WO_3 nanorods. Citric acid (Fig. 2a) promoted the formation of well-distributed particles of AgCl (indicated in pink color) and WO_3 (indicated in green color) with cubic to quasi-spherical shape ($d_{avg} = 4.6 \pm 1.1$ μm, Fig. 2b), and agglomerates of rods (as discussed later in Fig. 3), respectively. The spatial arrangement of AgCl and WO_3 is also confirmed by the SEM image and EDS spectrum from Fig. S3a, which shows that these particles are bound to each other. Similarly, the addition of Triton X-100 and PEG 2000 led to the formation of randomly distributed particles, with cubic to quasi-spherical AgCl (Fig. 2e,h and Fig. S3b-c) of average sizes of 5.2 ± 1.5 and 4.7 ± 1.1 μm, respectively. WO_3 (Fig. 2f,i) synthesized with both agents had a morphology similar to that of the material prepared in the absence of SDAs (Fig. S2c). The elemental mapping clearly shows that the ratio of AgCl to WO_3 particles was lower in the syntheses using these two agents compared to the final product of the synthesis using citric acid. It is expected that the conversion of the precursors to form WO_3 and AgCl and the relative growth rate of the two materials may be affected in different ways by the SDA. In this case, it is likely that citric acid facilitated the formation and growth of AgCl, resulting in a higher proportion of AgCl to WO_3 particles and achieving a better distribution [15].

Oxalic acid, in turn, induced the synthesis of WO_3 particles without a clear morphology, with a wide size range (29–142 μm), while the growth of AgCl particles was inhibited. In general, two different WO_3 structures were identified: (i) elongated grains of ~100 μm length with flat surfaces containing some grooves (Fig. 2k and EDS spectrum 3 of Fig. S3d); and (ii) smaller quasi-spherical bound particles with some nanorods grown on their surface (Fig. 2l and spectrum 2 of Fig. S3d). Unlike observed in the previous materials, the use of oxalic acid promoted the growth of AgCl over WO_3 in a considerably lower amount, as can be

Table 1
Lattice parameters, crystallite size, specific surface area from N_2-adsorption isotherms, band gap energy and absorption edge of the synthesized materials.

Sample	Lattice parameters (Å)		Crystallite size (nm)		Specific surface area ($m^2\ g^{-1}$)	Band gap energy, E_g (eV)	Absorption edge, λ (nm)
	a = b	c	WO_3[a]	AgCl[b]			
No SDA	7.40	3.91	20.2	56.2	29.51	2.88	432
Citric acid	7.43	3.93	33.7	59.8	4.48	2.93	423
Oxalic acid	7.41	3.92	26.3	58.9	4.02	3.20	388
Triton X-100	7.40	3.91	18.3	62.4	31.31	2.95	428
PEG 2000	7.44	3.92	19.2	63.3	16.37	2.96	419
Urea	7.15	3.86	–[c]	–[c]	0.19	2.91	426

[a]Calculated using the (0 1 0), (0 0 1) and (2 0 1) crystal planes; [b]Calculated using the (0 0 2) crystal plane; [c]The data did not allow calculating the parameter due to the poor definition of the XRD peaks.

better observed in Fig. S3d and its EDS spectrum 1. Similarly, urea also favored the synthesis of two different WO_3 structures, consisting of large, amorphous, WO_3 grains (Fig. 2n) and an ensemble of straight, regular, and laterally connected nanorods grown in the same direction (Fig. 2o). Once again, it is apparent that AgCl particles grew on the surface of WO_3 in smaller amounts (Fig. S3e), strengthening the interpretation of the XRD analysis, which showed the least intense characteristic peaks of AgCl ((1 1 1), (0 0 2), (0 2 2)) among all the samples prepared.

The WO_3-AgCl photocatalyst synthesized with citric acid was further analyzed by TEM, HRTEM, STEM-EDS and elemental mapping. Fig. 3a-b reveal that this material is composed of a combination of nanorods, with a length of 28 to 78 nm and width of 10 to 12 nm, and spheres with radius ranging from 4 to 20 nm. The high crystallinity of the catalyst was confirmed by the clear lattice boundary from the selected area analyzed by HRTEM (Fig. 3c). The lattice spacings of 6.32 Å, 2.04 Å and 2.36 Å corresponding to the crystalline planes (0 1 0) of hexagonal WO_3 (JCPDS Card No. 00–033-1387), (2 0 0) and (1 1 1) of silver (JCPDS Card No. 00–004-0783), respectively, can be identified in Fig. 3c.

The selected area in Fig. 3d clearly shows the presence of elements W, O, Ag, and Cl, observed by elemental mapping and STEM-EDS, in which W and O are concentrated in one spot, while Ag and Cl are in another spot, suggesting the formation of WO_3 and AgCl, respectively. The W and O elements seen in EDS spectra 2 and 4 of Fig. 3e-f confirm that the nanorods are indeed WO_3 particles. Other analyzed areas (spectra 1, 3 and 5 of Fig. 3e-g) reveal the presence mainly of Ag, with an almost insignificant peak for Cl, which means that they may refer to Ag particles. Therefore, SEM and TEM images suggest that the photocatalyst synthesized with citric acid is composed of nanosized Ag particles attached to the WO_3 nanorods, which are in contact with cube-like to nearly spherical AgCl particles of nano to micrometric sizes, suggesting the formation of a complex composite.

3.3. Specific surface area

The N_2-BET specific surface areas (SSA) of the photocatalysts synthesized with different SDAs are summarized in Table 1 (S_{BET}). Except for the material synthesized with Triton X-100, all structure-directing agents resulted in materials with significantly low SSA, all lower than that exhibited by the pure WO_3 (34.28 $m^2\ g^{-1}$). The SSA obtained with citric acid (4.48 $m^2\ g^{-1}$) and oxalic acid (4.02 $m^2\ g^{-1}$) can be attributed to the formation of larger crystals with a high degree of agglomeration, as previously discussed in the XRD and SEM results. The material prepared with Triton X-100 showed improved SSA, probably as a result of the stabilization of the WO_3 nanoparticles, which has also reflected in the smaller crystallite sizes observed. Regarding the sample modified with urea, the only material that was subjected to calcination, it is evident that the sharp reduction in S_{BET} occurred due to the thermal treatment, which promoted some degree of sintering, leading to pore collapse, and therefore, to a decrease in the specific surface area [28].

3.4. Valence states of surface-bound elements

An XPS analysis was performed to investigate the surface composition and chemical states of pure WO_3 and AgCl, and the WO_3-AgCl composite synthesized using citric acid, as depicted in Fig. 4. The data were adjusted to the C 1s position (284.8 eV) and the CasaXPS software was used for data fitting. The typical survey XPS spectrum (Fig. 4a) reveals that pure WO_3 contains mainly W and O, while the pure AgCl contains Ag and Cl; and the composite material is composed of all these four elements. The peak corresponding to Na observed in the spectra comes from the W precursor (sodium tungstate) used in synthesis. The chemical states of the elements were identified in the high-resolution XPS spectra of W 4f, O 1s, Ag 3d, and Cl 2p.

According to Fig. 4b, the two W 4f peaks of the composite material could be decomposed into four peaks: two strong peaks at 36.2 and 38.3 eV, corresponding to W $4f_{7/2}$ and W $4f_{5/2}$ of W^{6+}; and two smaller peaks at 35.0 and 38.7 eV, corresponding to W $4f_{7/2}$ and W $4f_{5/2}$ of W^{5+} [29,30]. Therefore, the surface of this material contains two valence states of tungsten [29], with oxygen vacancies [31]. For O 1s (Fig. 4c), a peak with maximum intensity at 530.9 eV can be observed, which was deconvoluted into three peaks at 530.6, 530.0 and 532.3 eV, assigned to the lattice oxygen of the O-W bond, adsorbed O_2, and to the OH^- groups (from absorbed water), respectively [29].

The two Ag 3d peaks of the bare AgCl (Fig. 4d) were split into two peaks at 367.7 and 373.7 eV, assigned to Ag $3d_{5/2}$ and Ag $3d_{3/2}$ of Ag^+ [32]. For the WO_3-AgCl sample, the same peaks can be identified, with a slight shift towards lower binding energies (367.3 and 373.3 eV). Additionally, two small shoulders at the peak of the WO_3-AgCl sample could be assigned to Ag $3d_{5/2}$ and Ag $3d_{3/2}$ of Ag^0, at 367.9 and 374.0 eV [33], corroborating the results from the TEM analyses (Fig. 3), where Ag^0 was identified. In Fig. 4e, two Cl 2p peaks in the bare AgCl sample, at 198.0 and 199.7 eV were assigned to Cl $2p_{1/2}$ and Cl $2p_{3/2}$ of Cl^- [29]. The same peaks were identified in the WO_3-AgCl sample, with a slight shift toward lower binding energies, that is, 197.7 and 199.4 eV.

3.5. Optical properties

UV–vis diffuse reflectance spectra (DRS) were used to investigate the optical properties of the synthesized materials, as depicted in Fig. 5a. Due to the significant absorption in the ultraviolet (UV) region and some absorption in the visible range, all photocatalysts exhibited broad-spectrum activity. The band gap energies were estimated by the Tauc plot derived from the Kubelka-Munk function, extrapolating a straight line from the linear section to the intersection of the *x*-axis [34]. Eq. (1) is used for this purpose, where h is the Planck constant, ν is the photon frequency, B is the proportionality constant, E_g is the band gap energy, and n is a factor associated with the nature of the electron transition (1/2 for direct and 2 for indirect transition band gaps. $F(R)$ is the Kubelka-Munk function, described by Eq. (2), where K is the absorption coefficient and S is the scattering coefficient [35]. Fig. 5b shows the Tauc plots, and the calculated bandgap energies are included in Table 1. The E_g values are observed to have ranged from 2.87 to 3.20 eV, indicating

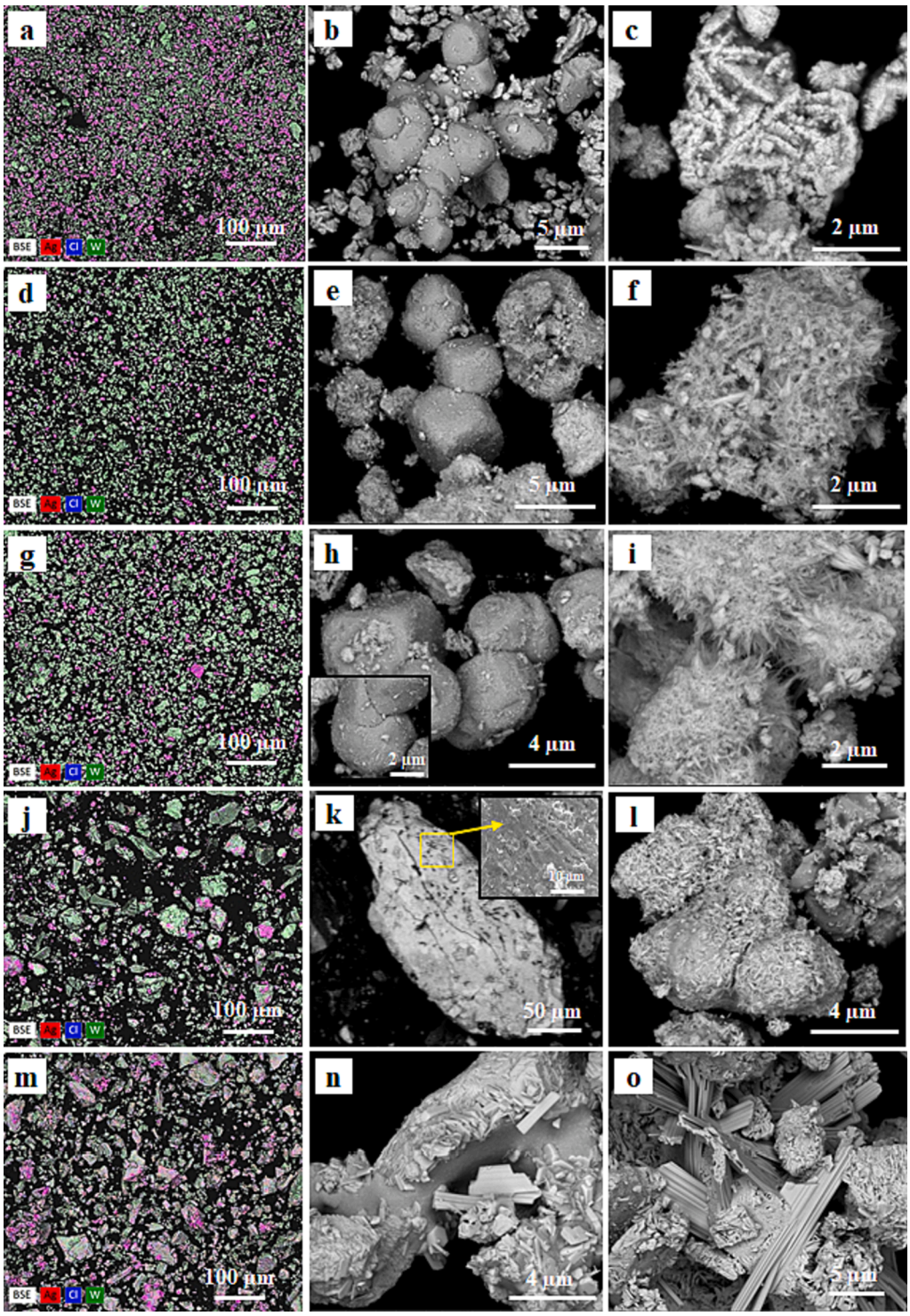

Fig. 2. SEM images of WO_3-AgCl photocatalysts synthetized by the hydrothermal method using a-c) citric acid, d-f) Triton X-100, g-i) PEG 2000, j-l) oxalic acid, m-o) urea.

that, in general, the values increased slightly with the addition of structure-directing agents, especially when oxalic acid was used. However, there was no significant variation in E_g values for the modified materials.

$$(F(R)h\nu)^{1/n} = B(h\nu - E_g) \quad (1)$$

$$F(R) = \frac{K}{S} \quad (2)$$

Furthermore, the DRS spectra (Fig. 5a) clearly indicate the presence of an LSPR (localized surface plasmon resonance) peak at 537 nm, especially evident in the sample synthesized with citric acid. LSPR is an optical phenomenon that results from interactions between incident photons and electrons in the conduction band of a noble metal nanostructure. This interaction results in a collective oscillation of valence electrons and subsequent absorption within the ultraviolet–visible (UV–vis) band [36]. In other words, when light hits the surface of the noble metal, it is scattered and absorbed on its surface, creating an

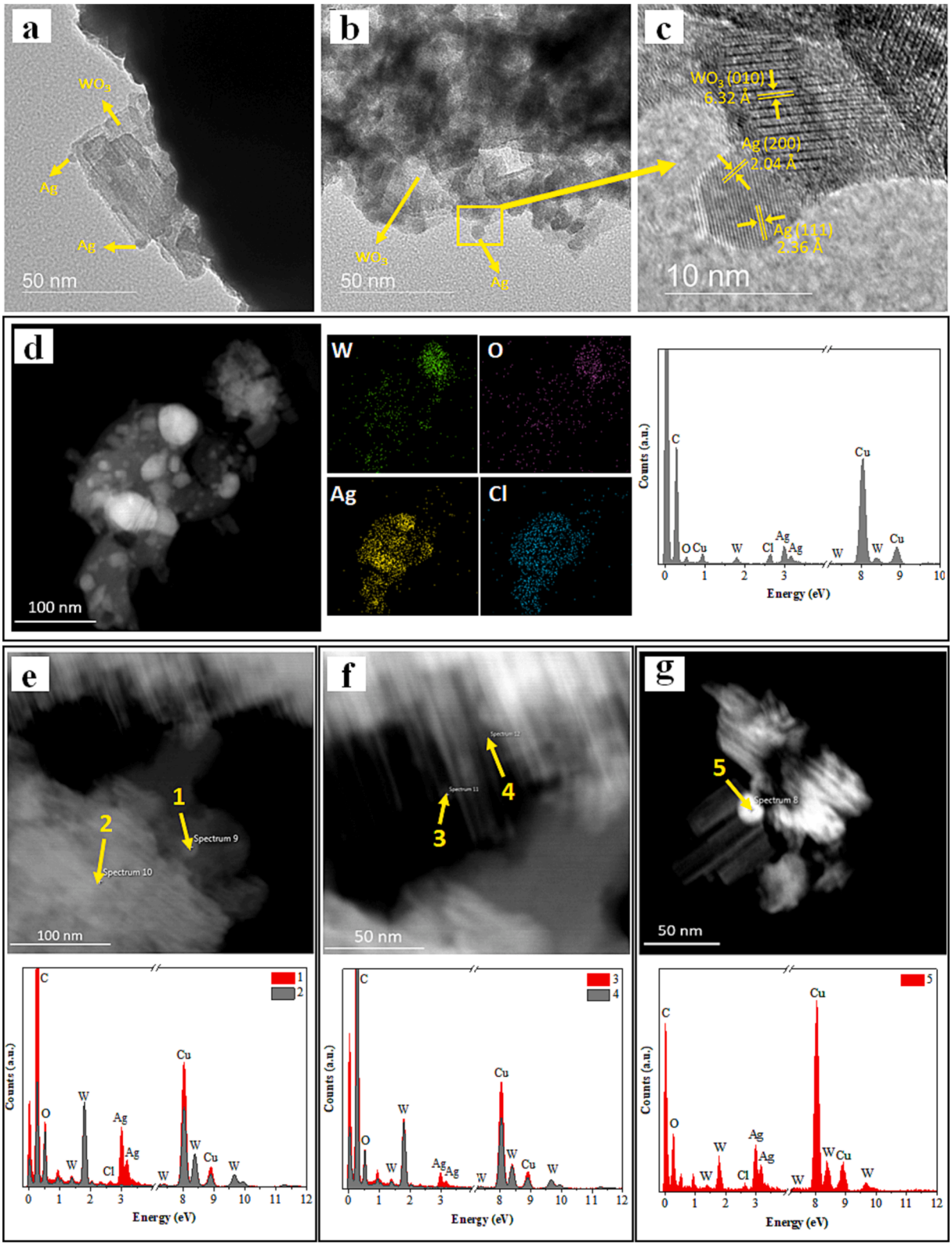

Fig. 3. a-b) TEM imagens; c) HRTEM image; d) STEM image and its respective elemental mapping and EDS spectrum; e-g) STEM images and their respective eds spectra of the WO_3-AgCl photocatalyst synthesized with citric acid. All samples were deposited on a Cu mesh.

evanescent wave with a strong electromagnetic field localized on the particle surface, staying at a distance from the surface smaller than the diameter of the nanoparticle [37]. As a consequence, the light absorption is enhanced and the separation of e^-/h^+ pairs is accelerated by the strong magnetic field, thus, increasing the photocatalytic activity of the composite material [6,7]. Therefore, the presence of the LSPR peak corroborates the results discussed previously, implying that the Ag particles observed by STEM-EDS and XPS (Figs. 3-4) are responsible for promoting the effect of plasmonic resonance in the material. Chen et al. [38], for example, synthesized Ag/AgCl coupled to WO_3 and observed a

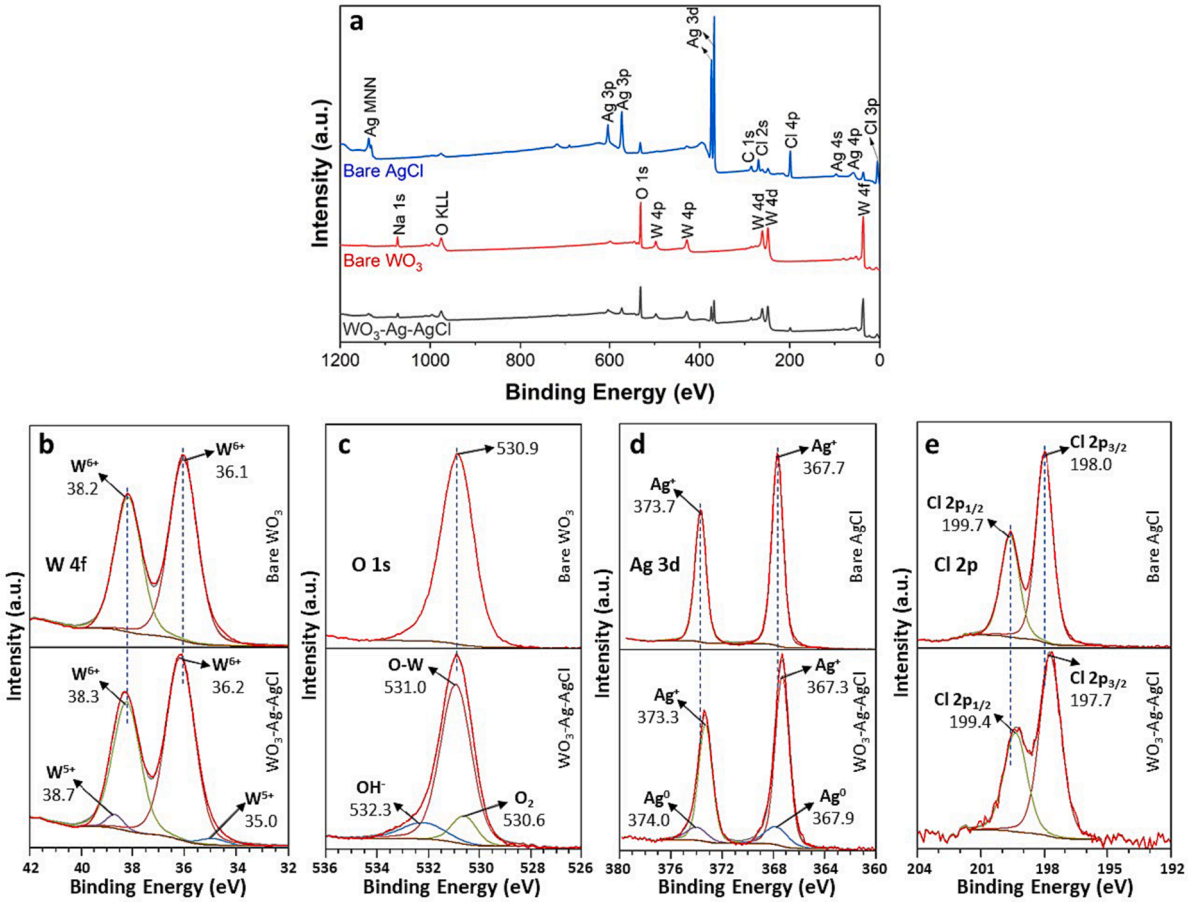

Fig. 4. XPS spectra of the bare WO_3, bare AgCl, and WO_3-AgCl photocatalyst synthesized with citric acid a) survey, b) W 4f, c) O 1s, d) Ag 3d and e) Cl 2p.

broad absorption band from 420 to 800 nm, which was also attributed to the LSPR effect.

In addition, photoluminescence (PL) was evaluated to provide information on defect levels and gap states, since it is highly affected by the impurities and defects in the semiconductor structure [39]. The normalized PL spectra (Fig. 5c), measured at an excitation wavelength of 370 nm, show emission peaks with the highest intensities at 442, 470 and 431 nm for the bare WO_3, bare AgCl and WO_3-AgCl catalyst synthesized in the presence of citric acid, respectively. The bare WO_3 and AgCl present broader bands covering from violet to green emissions, while the WO_3-AgCl material covers mainly violet-blue emissions. According to Longo et al. [40], the violet and blue emission can be attributed to surface defects within the band gap and a more organized structure; while the green, yellow, and red emission is associated with defects located deeper within the band gap and a higher level of disorder in the lattice. Thus, each color describes a distinct type of electronic transition and is correlated with a particular structural configuration [40]. Further analyses must be carried out to better assess the type of defect that occurs in each material. Even so, it is known that these defects act as radiative centers in the luminescence process and can serve as a hole-trapping state in semiconductors [41,42].

To better understand the photoluminescence results, the time-resolved PL decay (logarithmic scale), depicted in Fig. 5d, was measured using a laser emitting at 355 nm. The time-resolved PL on a linear scale is shown in Fig. S4. Clearly, the WO_3-AgCl photocatalysts synthesized with different structure-directing agents exhibited different decay behavior compared to pure WO_3, indicating longer emission lifetimes. Initially, a fast decay can be observed, followed by at least three other slower decays, which are more evident for the WO_3-AgCl materials (Fig. 5d). Note that the sample synthesized with oxalic acid showed the fastest decay of all composites, which serves as further evidence for the poor photocatalytic activity of this material, as discussed later.

3.6. Photocatalytic activity

The effect of different SDAs on the photocatalytic activity of synthesized WO_3-AgCl materials was evaluated on acetaminophen degradation under simulated sunlight. Photolysis of ACT showed 8.2% of removal (Fig. S5a), while experiments carried out in the dark with the synthesized photocatalysts demonstrated that there was no significant ACT adsorption (Fig. S5b). Pure WO_3 and AgCl, synthesized using the same methodology, showed 15.5% and 77.1% of ACT removal after 120 min of reaction (Fig. S6), respectively. It is important to note that while pure AgCl leads to high removal rates, since it is not a stable material, it might lose its photocatalytic efficiency with further uses [38]. Fig. 6 shows the photodegradation performance, measured after 120 min, and the corresponding pseudo first-order specific degradation rates, which together indicate that the addition of SDA to the synthesis has a strong influence on the photocatalytic activity. The addition of PEG 2000 resulted in 94.30 ± 0.04% ACT removal (k = 0.052 min^{-1}), a lower photocatalytic performance than that of the material without SDA (99.60 ± 0.10% ACT removal; k = 0.063 min^{-1}). Similar results were obtained for the material synthesized with Triton X-100, which resulted in the removal of 98.55 ± 0.01% ACT (k = 0.046 min^{-1}). Triton X-100 and PEG 2000 may have acted similarly during the crystal nucleation and growth stages, resulting in morphologically similar materials. In addition, the two catalysts did not differ much morphologically from the material synthesized in the absence of SDAs, which may explain their similar photocatalytic activity.

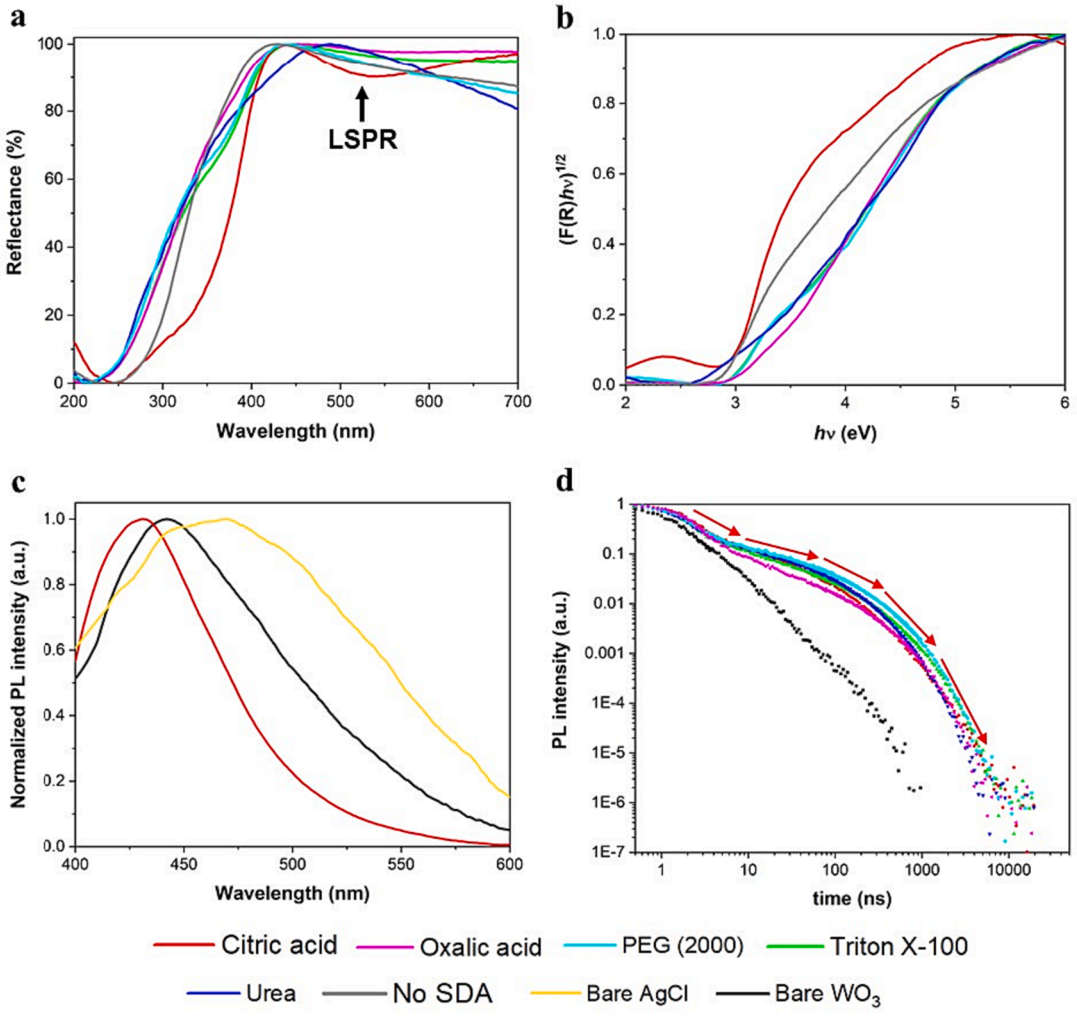

Fig. 5. A) UV–vis diffuse reflectance spectra (DRS); b) Tauc plot of WO_3-AgCl photocatalysts synthesized with different structure-directing agents (SDA); c) Normalized photoluminescence spectra of some specific materials; and d) Time-resolved photoluminescence decay on a logarithmic scale.

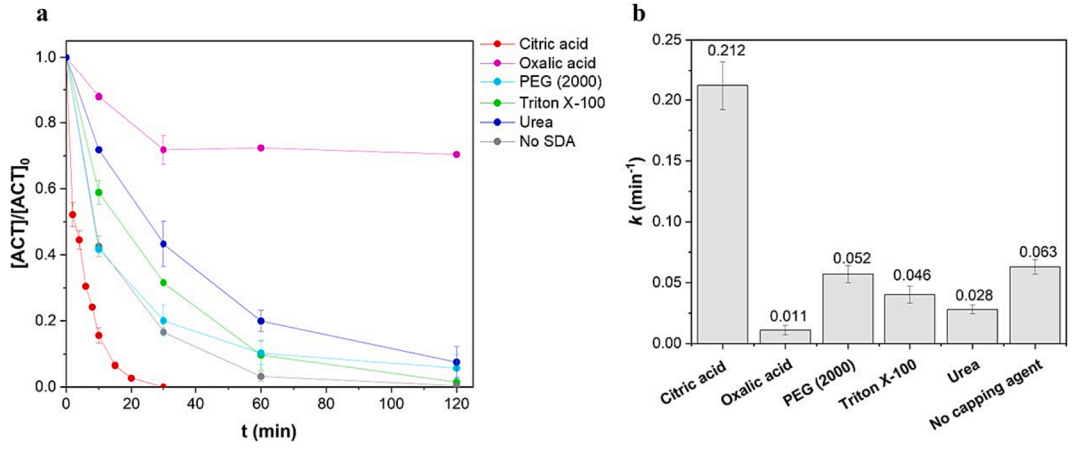

Fig. 6. a) Performance of WO_3-AgCl photocatalysts synthesized with various structure-directing agents in the photocatalytic degradation of acetaminophen ($[ACT]_0 = 4.95 \pm 0.88$ mg L^{-1}) under simulated sunlight; and b) Corresponding pseudo first-order specific degradation rates.

The catalyst synthesized in the presence of urea slightly hindered the removal of ACT compared to the material synthesized without SDAs, reaching a removal of 92.50 ± 0.04% ($k = 0.028$ min^{-1}), which may be due to its low SSA and the presence of rather large WO_3 particles. However, the AgCl particles spread throughout the WO_3 surface, influencing the good photocatalytic activity. The low photocatalytic activity of the material synthesized with oxalic acid (29.62 ± 0.001% ACT removal; $k = 0.011$ min^{-1}), conversely, can be explained by the poor distribution of particles, the low SSA, the considerably high band gap energy, and also the possible presence of residual oxalate adsorbed

on the catalyst surface, acting as a hydroxyl radical scavenger [43]. Finally, the highest photocatalytic performance was observed with the catalyst synthesized with citric acid, achieving ACT removal of 100.0% after 30 min ($k = 0.212$ min^{-1}). This superior performance may be due to the perfect distribution of AgCl and WO_3 particles, and mainly to the presence of AgCl in a higher amount when compared to other materials. Furthermore, the presence of an LSPR peak for the material synthesized with citric acid (Fig. 5a) may also have strongly contributed to the increase in photocatalytic activity. It is important to point out that the experiments carried out with this material lasted only 30 min, as the ACT concentration was below the limit of quantification for longer reaction times.

4. Discussion

4.1. Effect of structure-directing agents

In the present work, structure-directing agents of different molecular structures, such as organic acids (citric and oxalic acids), surfactants (Triton X-100, PEG 2000) and one nitrogenous compound (urea) were used to evaluate their effect on the hydrothermal synthesis of WO_3 coupled to AgCl. According to the results above, the addition of these SDA can strongly influence the morphology of the synthesized photocatalysts. Organic acids can act as protective ligands to stabilize crystal growth [31]. Oxalic and citric acids are polycarboxylic and hydroxy-polycarboxylic acids, respectively; i.e., oxalic acid has two carboxyl (–COOH) groups, while citric acid has three carboxyl groups and one hydroxyl (–OH) group [13,15]. The synthesis of photocatalysts is guided by nucleation and crystal growth processes. However, the nucleation rate can be modified by these carboxylic acid complexes. In aqueous solutions, these acids are known to form chelates with tungsten species with –O–W–O linkage, making tungsten solutions stable and preventing WO_4^{2-} polycondensation [15]. In the initial stage, when tungsten oxide hydrate seed particles are produced, the acids selectively bind to the particular facets of the seeds and stabilize the specific planes. In other words, the relative growth of different facets is influenced by the alternation in the order of free energies of the various facets of the seed surface through weak and strong bindings [15,44]. Likewise, oxalic and citric acids could selectively bind AgCl seeds, retarding grain growth [45,46]. Li et al. [31] claim that oxalic acid can stabilize the structures and inhibit the stacking of WO_3. Surprisingly, in our work, oxalic acid strongly inhibited AgCl particle formation and led to exaggerated growth of WO_3 particles (Fig. 2j-l). Nevertheless, a certain amount of oxalic acid can prevent the particles from crystallizing and growing [31]. Conversely, citric acid probably led to the same growth rate for AgCl and WO_3, which facilitated the synthesis of well-distributed particles. This difference may be related to the presence of an extra hydroxyl group and a carboxyl group in citric acid, which can release H^+ allowing it to bond with metallic hydroxides.

Surfactants can enhance the materials because of their amphiphilic nature. Triton X-100, for example, has a hydrophilic polyethylene glycol chain and a lipophilic hydrocarbon chain. During the synthesis procedure, part of Triton X-100 can be selectively adsorbed into the crystallite structure, inhibiting ions, such as W^{6+} and O^{2-}, from coming into contact with the crystal surface [19,23]. Adsorbed Triton X-100 molecules could play an important role in decreasing the growth rate of crystal faces where adsorption occurs [19]. In our work, Triton X-100 guided the synthesis of less aggregated AgCl particles and agglomerates of WO_3 nanorods, but still quite similarly to the unmodified material (Fig. 2d-f). PEG, in turn, is a hydrophilic linear chain polymer whose physical properties depend on its molecular weight [24]. The polymer molecules can form hydrogen bonds with the WO_3 particles and thus the polymer chain will start to spread out, preventing other chains from connecting to the photocatalyst particles. These chains are shorter for lower molecular weight polymers [47]. In the synthesis of WO_3 coupled to AgCl, PEG 2000 did not significantly affect the morphology of the catalysts, compared to the unmodified material (Fig. 2g-i). According to Sudha et al. [47], PEG with higher molecular weights (> 600 g mol^{-1}) may not significantly influence material growth because nanoparticles can adsorb a smaller amount of polymer.

Finally, it is known that urea plays an important role in crystal growth in hydrothermal synthesis. When crystal growth is initiated, the pH of the system increases due to the decomposition of urea, preventing the growth of WO_3. Under hydrothermal conditions, urea hydrolysis can occur, generating NH_4^+ and HCO_3^- and slowly modifying the pH [48]. According to Zheng et al. [48], the presence of NH_4^+ and the appropriate pH value during the slow growth process can lead to the formation of hexagonal WO_3. At the same time, the thickness of the particles may be limited by the adsorption of CO_3^{2-} or HCO_3^- on the surface of WO_3, which may explain the formation of a group of straight, regular, and laterally-connected nanorods grown in a similar direction when urea was used, instead of nanorods (Fig. 2m-o). The absence of quasi-spherical AgCl particles in the catalyst can be explained because urea hindered the growth of AgCl crystallites.

4.2. Photocatalyst stability

Due to the superior photocatalytic performance of the material synthesized with citric acid, it was further analyzed through some extra characterization techniques and photocatalytic tests. First, its stability was evaluated by reuse tests of 20 min each, as described elsewhere [4]. As can be seen in Fig. 7a, the ACT removal capacity was reduced by 18.8% after 4 cycle times, indicating good stability. Fresh and used materials were analyzed by XRD and, according to Fig. 7b, their composition remained practically unchanged during the photocatalytic experiments. However, the reused catalyst presented three extra peaks at $2\theta = 38.1°$, 44.3°and 64.4° indexed to the planes (1 1 1), (2 0 0) and (2 2 0) of cubic Ag (JCPDS Card No. 00–004-0783). This implies that during the photodegradation experiments, some Ag^+ ions may have been reduced to Ag^0 by electrons in the conduction band and/or photo-reduced [49]. The reused material was also inspected by TEM (Fig. S7), revealing nanorods (WO_3) and darker quasi-spherical particles (AgCl and Ag), as already observed in the fresh catalyst (Fig. 3), indicating that few morphological changes occurred during treatment cycles.

4.3. Effect of the water matrix

The catalyst synthesized with citric acid was also evaluated in photocatalytic assays using real effluent from a pharmaceutical industry that produces different pharmaceuticals, including ACT. The effluent, whose characterization is shown in Table S1, was collected after the primary treatment process of a pharmaceutical facility and spiked with ACT to reach a final concentration of 5 mg L^{-1}. Photodegradation experiments were performed as previously described, and, after 20 min of reaction, 83.60 ± 0.01% ACT removal ($k = 0.061$ min^{-1}) was obtained (Fig. 7c), indicating a reduction of 14.1% in ACT removal compared to the assay using ultrapure water. This hindrance in removal capacity in real wastewater is expected and may be primarily related to the presence of competing chemicals in the effluent, as evidenced by its high chemical oxygen demand (87.2 mg L^{-1}) and total suspended solids (88 mg L^{-1}).

4.4. Photocatalytic test under continuous regime

To assess the possibility of applying this material in a continuous regime, an additional experiment was carried out in continuous flow using the optimal catalyst (i.e., synthesized with citric acid). 30 mg of this material was packed into a capillary tube ($d_{int} = 1.0$ mm; length = 75 mm) as micro packed-bed reactor [50], resulting in a bed approximately 25 mm long (Fig. 8). The reactor was placed under the irradiation source under the same conditions as in the batch assays, and the ACT solution (prepared with ultrapure water with an initial concentration of 5 mg L^{-1}) was continuously pumped through the reactor with a space

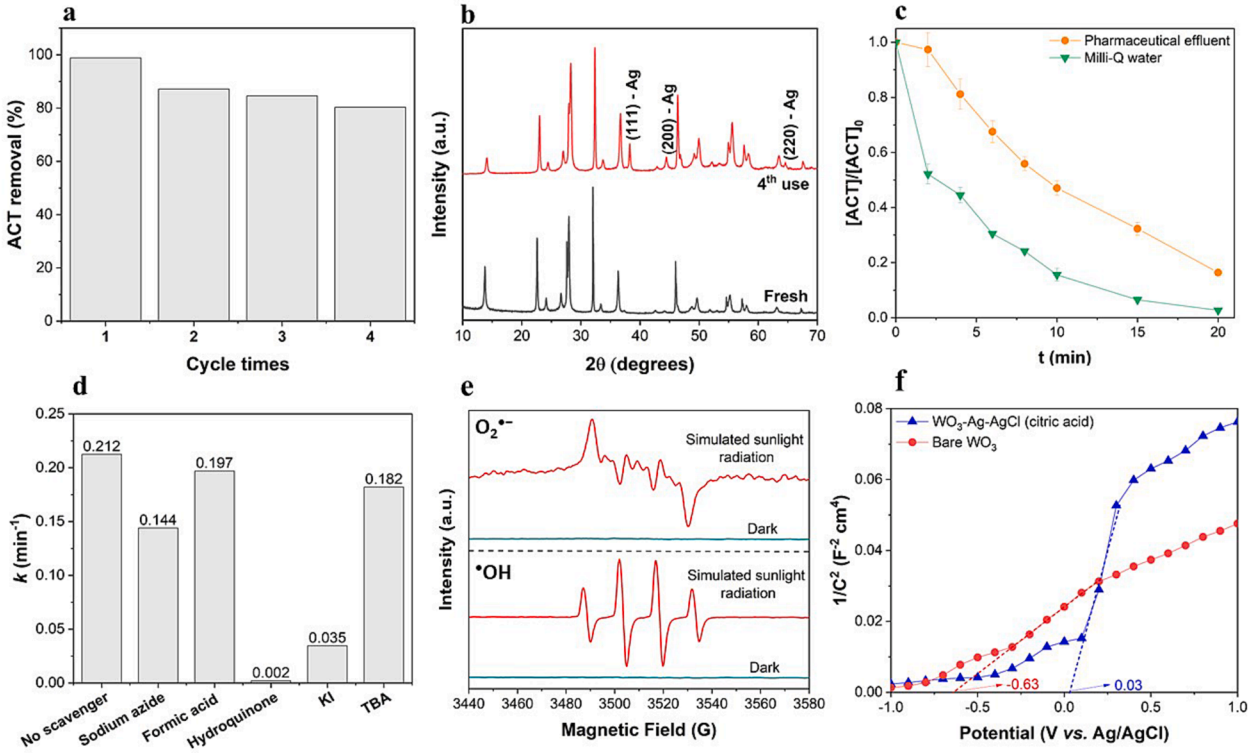

Fig. 7. A) Reuse tests of the photocatalyst synthesized with citric acid after 20 min of reaction of each run; b) XRD diffraction peaks of the fresh and used photocatalyst; c) Effect of water matrices in photocatalytic assays using the photocatalyst synthesized with citric acid; d) Effect of radical scavengers on the efficiency of ACT removal using the WO_3-AgCl (citric acid) catalyst. Conditions: $[ACT]_0 = 5.31 \pm 0.63$ mg L^{-1}, $m_{catalyst} = 10$ mg, $V_{solution} = 10$ mL; scavenger dosage = 0.02 mol L^{-1}, irradiation time = 20 min; e) EPR spectra of $^{\bullet}OH$ radicals trapped by DMPO in aqueous medium and $O_2^{\bullet-}$ radicals trapped by DMPO in methanol medium using the WO_3-AgCl (citric acid) catalyst under simulated solar radiation. Conditions: [catalyst] = 1 mg mL^{-1}, $[DMPO]_{\bullet OH} = 50$ mmol L^{-1}, $[DMPO]_{O2\bullet-} = 100$ mmol L^{-1}, irradiation time = 15 min; f) Mott-Schottky curves.

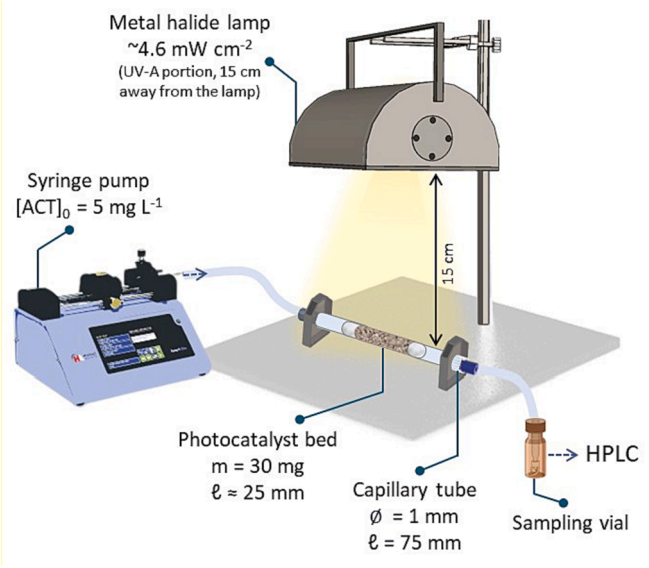

Fig. 8. Experimental apparatus for the continuous photocatalytic tests.

time of 5 min. A steady-state ACT removal of 97.9% was obtained, demonstrating that the synthesized material presented high photocatalytic activity in the continuous regime.

4.5. Effect of oxidizing species

In order to understand the reactive oxidizing species participating in the photocatalysis mechanism, some additional tests were performed with radical scavengers and the material synthesized with citric acid. Hydroxyl radicals ($^{\bullet}OH$), superoxide radical anions ($O_2^{\bullet-}$), holes in the valence band (h^+), and electrons in the conduction band (e^-) are recognized to be the main active species in photocatalytic systems [4,51]. Thus, the radical scavengers formic acid, *tert*-butanol (TBA), 1,4-hydroquinone, potassium iodide (KI) and sodium azide were used, with an initial concentration of 0.02 mol L^{-1} for each quencher. The data fitted to the pseudo first-order kinetics and, according to Fig. 7d, the inhibition of the ACT removal rate was: 99.1% with 1,4-hydroquinone > 83.5% with KI > 32.1% with sodium azide > 14.2% with TBA > 7.1% with formic acid. 1,4-hydroquinone is a good scavenger of $O_2^{\bullet-}$ ($k = 1.6 \times 10^7$ L mol^{-1} s^{-1}) and $^{\bullet}OH$ radicals ($k = 2.1 \times 10^{10}$ L mol^{-1} s^{-1}) [52]. KI is usually used to scavenge h^+, since iodine donates electrons to valence band holes in the material; yet, it is also a good scavenger of $^{\bullet}OH$ radicals [53]. TBA quickly reacts with $^{\bullet}OH$ ($k = 4.2$–7.6×10^8 L mol^{-1} s^{-1}) [54,55], whereas sodium azide, although commonly used as an e^- scavenger, can also quench $^{\bullet}OH$ radicals [53]. Formic acid, in turn, can react with h^+ [53,56] and also with $^{\bullet}OH$ with a high rate constant ($k = 1.2 \times 10^8$ L mol^{-1} s^{-1}) [57]. Therefore, these results indicate that $^{\bullet}OH$, $O_2^{\bullet-}$ and h^+ are the main reactive species present in ACT degradation.

EPR studies were performed using DMPO (5,5-dimethyl-1-pyrroline N-oxide) as a spin-trapping agent to better understand the radical species involved in the reactions, as described elsewhere [22]. For the detection of $^{\bullet}OH$ radicals, 50 mmol L^{-1} of DMPO was used in aqueous medium, while 100 mmol L^{-1} of DMPO in methanol medium was applied for detecting $O_2^{\bullet-}$. Fig. 7e reveals that under dark conditions, no peaks could be detected, as expected. The four characteristic peaks of the DMPO-$^{\bullet}OH$ adduct confirm the presence of hydroxyl radicals in the photodegradation reaction. Regarding $O_2^{\bullet-}$ detection, the six characteristic peaks of the DMPO-$O_2^{\bullet-}$ adduct are not perfectly assigned due to

the instability of this radical, but it is still possible to notice this adduct pattern [22,58]. Therefore, these results confirm the participation of both $^{\bullet}OH$ and $O_2^{\bullet-}$ radicals in the photocatalytic degradation of ACT using the WO_3-AgCl catalyst synthesized with citric acid.

4.6. Photodegradation mechanism

Mott-Schottky analyses were carried out to obtain the band edge positions of the materials [59]. The plots of the bare WO_3 and the composite material synthesized with citric acid show a positive slope for both materials (Fig. 7f), characteristic of *n*-type semiconductors [60]. The Mott-Schottky equation (Eq. (3) was used to estimate the flat band potential (E_{FB}), where C is the interfacial capacitance, ε is the vacuum permittivity, ε_0 is the relative permittivity of the material, A is the area, N_D is the number of donors, V is the applied voltage, k_B is Boltzmann's constant, T is the absolute temperature, and e is the electronic charge [61].

$$\frac{1}{C^2} = \frac{2}{\varepsilon\varepsilon_0 A^2 e N_D}\left(V - E_{FB} - \frac{k_B T}{e}\right) \quad (3)$$

The term k_BT/e is generally considered negligible and therefore the flat band potential (E_{FB}) can be estimated by extrapolating the linear portion of the Mott-Schottky plot on the x axis, which is then converted using the formula $E(\text{NHE}) = E(\text{Ag/AgCl}) + E^{\theta}$ [61], where E(Ag/AgCl) is the potential obtained by the graph and E^{θ} (Ag/AgCl) = 0.197 V. The flat band potentials obtained for the bare WO_3 and WO_3-AgCl (citric acid) are −0.433 and 0.227 V vs. NHE, respectively. It is generally assumed that the E_{FB} for *n*-type semiconductors is the same as the conduction band (CB) or about 0.1–0.2 eV smaller than the CB [62]. Therefore, it can be assumed that the CB position of the bare WO_3 synthesized in the present work is in the range −0.433 to −0.633 V, and 0.227 to 0.027 V for WO_3-AgCl (citric acid); while the VB position is in the range 2.247 to 2.447 V for WO_3 and 2.957 to 3.157 V for WO_3-AgCl (citric acid). Based on this information, the band edge diagram of both samples is presented in Fig. 9, which shows that both the conduction and valence bands are pushed to higher potentials for the composite material; a similar behavior was observed by Kalanur [59], who synthesized Sn-doped WO_3. According to the VB position, $^{\bullet}OH$ radicals can be formed by the reaction of accumulated holes with H_2O or OH^- ($^{\bullet}OH/H_2O = 2.72$ eV vs. NHE; $^{\bullet}OH/OH^- = 2.40$ eV vs. NHE) [22] for the WO_3-AgCl (citric acid) catalyst. The CB position of WO_3-AgCl (citric acid), however, does not favor the formation of superoxide radicals ($O_2/O_2^{\bullet-} = -0.33$ eV vs. NHE) [22]. Even so, $O_2^{\bullet-}$ radicals could be generated by the reaction of accumulated electrons with O_2, since the reference potentials cited above are estimated on the basis of the standard temperature and activities of the species involved and may differ from the actual conditions applied to the process [22]. The charge carrier separation efficiency of the composite material was confirmed by time-resolved PL, which showed longer lifetimes for the WO_3-AgCl materials compared to bare WO_3. Although the band edge diagram of WO_3-AgCl (citric acid) estimated from the Mott-Schottky analysis indicates that $O_2^{\bullet-}$ radicals cannot be formed, this goes against the results of EPR measurements and radical scavenger tests. However, the flow of electrons and holes, and consequently, the formation of radicals, especially $O_2^{\bullet-}$, generates much debate and various uncertainties [63].

Still, two possible reaction mechanisms for the WO_3-AgCl (citric acid) catalyst are proposed based on our results and previous studies (Fig. 9). Silver particles on the surface of WO_3 are suggested due to evidence from HRTEM and XPS analyses, while Ag particles on the surface of AgCl and in contact with both AgCl and WO_3 are proposed due to the photo-reduction of Ag^+ from AgCl, observed by the XRD of the used material. These Ag particles can promote the LSPR effect on the surface of the semiconductors, as indicated by the UV–vis DRS results, allowing both AgCl and WO_3 to efficiently absorb visible light. The photocatalytic reaction begins with the absorption of photons with energy equal to or greater than the band gap energies of WO_3 and AgCl, resulting in the generation of e^-/h^+ pairs (Eqs. (4)–(5). Apart of charge carrier recombination, and assuming that the transfer of charge carriers follows the type II heterojunction, the photogenerated h^+ can be transferred from the VB of WO_3 to the VB of AgCl; these accumulated holes

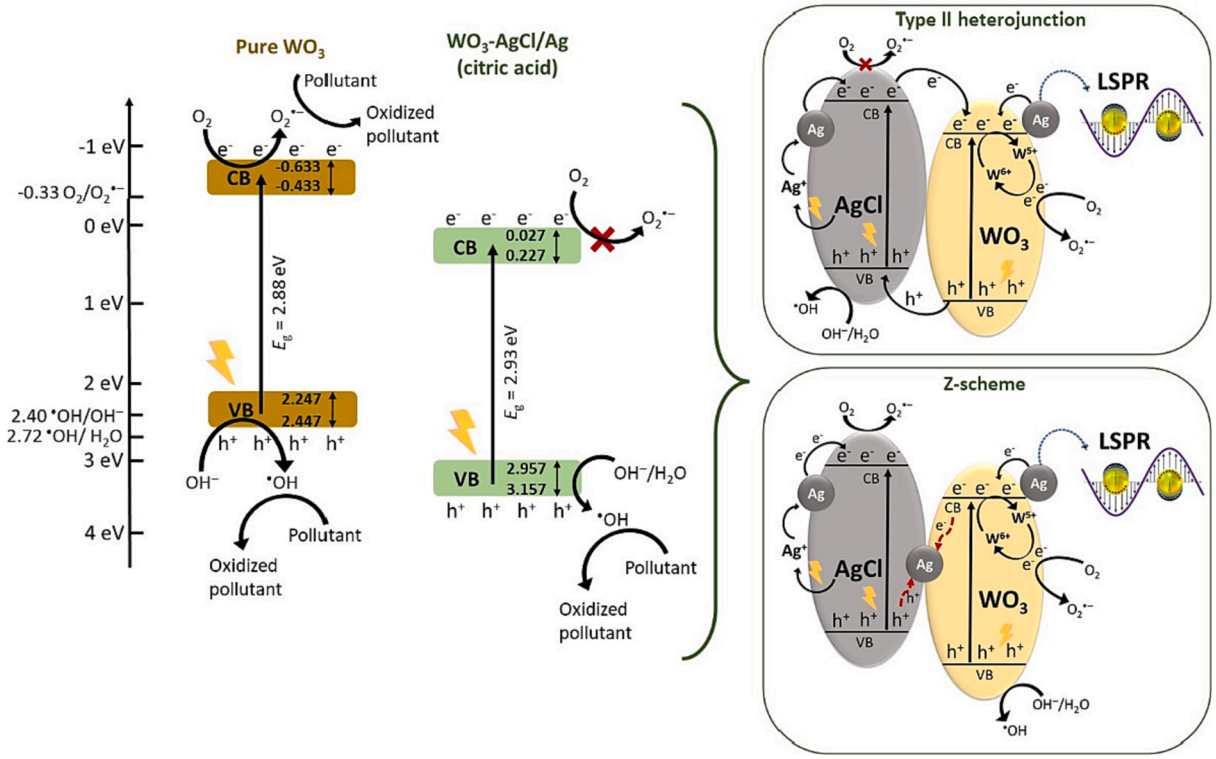

Fig. 9. Band edge diagram for the bare WO_3 and WO_3-AgCl (citric acid) catalysts (left) and proposed reaction mechanisms (right).

can react with H_2O or OH^- to generate $^{\bullet}OH$ radicals (Eqs. (6)–(7). At the same time, the e^- from the plasmonic Ag can flow to both AgCl and WO_3 due to the LSPR effect [7]; while the e^- accumulated in the CB of AgCl can migrate to the CB of WO_3. As a result, most of the electrons are accumulated in the CB of WO_3, which is known to be more positive than the $O_2/O_2^{\bullet-}$ redox potential [22]. The impossibility of $O_2^{\bullet-}$ formation, however, is inconsistent with our experimental results for radical scavengers.

Another charge carrier transfer alternative to help elucidate the enhanced photocatalytic performance of WO_3/AgCl (citric acid) would be the Z-scheme, in which metallic Ag is situated between AgCl and WO_3, acting as an electron-conduction bridge [64]. Plasmonic silver on the surface of WO_3 and AgCl is also accepted in this mechanism, as discussed in the type II heterojunction. It should be noted that plasmonic Ag plays an important role in the reaction rate in both mechanisms, since its strong electromagnetic field can accelerate the separation of e^-/h^+ pairs [7]. The electrons in the CB of WO_3 and the holes in the VB of AgCl will migrate to metallic Ag through the Schottky barrier, resulting in their recombination [64]. Due of the more negative position of the CB of AgCl, the electrons concentrated there would have a greater chance of reacting with O_2, generating $O_2^{\bullet-}$ radicals (Eq. (8); while the holes accumulated in the VB of WO_3 will produce $^{\bullet}OH$ (Eqs. (6)–(7). In addition, the generation of $O_2^{\bullet-}$ may be related to the occurrence of defects with intermediate energies, in both proposed mechanisms. W^{5+} can be photoexcited, generating W^{6+} and photogenerated electrons (Eq. (9), which can lead to the formation of $O_2^{\bullet-}$ radicals, since the electrons are trapped by the adsorbed O_2. The photocatalytic cycle is completed as W^{6+} reacts with OH^- and is reduced to W^{5+}, yielding $^{\bullet}OH$ radicals (Eq. (10) [22,29,65]. After all, $^{\bullet}OH$, $O_2^{\bullet-}$ and h^+, the main reactive species identified in experiments with radical scavengers, would be available for the degradation of ACT (Eqs. (11)–(13). It is important to emphasize that further analyses should be carried out to confirm whether the mechanism is more likely to occur.

$$WO_3 + hv \rightarrow WO_3(e^-) + WO_3(h^+) \quad (4)$$

$$AgCl + hv \rightarrow AgCl(e^-) + AgCl(h^+) \quad (5)$$

$$H_2O + h^+ \rightarrow \cdot OH + H^+ \quad (6)$$

$$OH^- + h^+ \rightarrow \cdot OH \quad (7)$$

$$O_2 + e^- \rightarrow O_2^{\cdot-} \quad (8)$$

$$W^{5+} + hv \rightarrow W^{6+} + e^- \quad (9)$$

$$W^{6+} + OH^- \rightarrow W^{5+} + \cdot OH \quad (10)$$

$$h^+ + ACT \rightarrow degradation\ products + CO_2 + H_2O \quad (11)$$

$$\cdot OH + ACT \rightarrow degradation\ products + CO_2 + H_2O \quad (12)$$

$$O_2^{\cdot-} + ACT \rightarrow degradation\ products + CO_2 + H_2O \quad (13)$$

4.7. Comparison with previous studies

Modification of the WO_3 with various transition and noble metals, non-metals, and coupling the material with other semiconductors to form heterojunctions has been widely explored [66]. Table 2 presents a brief comparison of some recently reported WO_3-based photocatalysts for wastewater treatment purposes. Although different synthesis methods have been applied, the hydrothermal method is commonly used due to its simplicity. Regardless of the type of structure formed, all materials showed good photocatalytic activity with an irradiation source simulating the sunlight spectrum. Among the various contaminants studied, ranging from dyes to pharmaceuticals, degradation rates greater than 65% could be obtained with the WO_3-based materials, reinforcing their higher photocatalytic activity. When comparing reaction times in general, at least 60 min of reaction is required to lead to a high contaminant removal, i.e., greater than 80%. In our previous study, where the temperature and time of synthesis were optimized, 99.6% of acetaminophen removal was obtained after 120 min of reaction, under the optimum condition [22]. Here, these conditions were further improved by the addition of structure-directing agents to the catalyst, and finally, 100.0% acetaminophen removal was achieved after only 30 min of reaction, with the photocatalyst synthesized with citric acid. This result reinforces the importance of adding SDA, especially citric acid, in the synthesis step. It is worth noting that none of the studies reported in Table 2 used any type of SDA in their synthesis, which might have led to this considerable difference in the photocatalytic activity.

5. Conclusions

In this work, citric acid, oxalic acid, urea, polyethylene glycol, and Triton X-100 were used as structure-directing agents in the synthesis of WO_3-AgCl photocatalysts by a simple one-step hydrothermal method. The photocatalyst synthesized with citric acid resulted in the best distribution of WO_3 and AgCl particles, with some Ag particles between the WO_3 layers. The lifetime of the composites was improved compared to the bare WO_3 photocatalyst. The photocatalytic efficiency of the

Table 2
Comparison of different WO_3-based photocatalysts and their application in heterogeneous photocatalysis.

Photocatalyst	Synthesis method	Irradiation source	Model contaminant / initial concentration	Photocalyst mass / contaminant volume	Maximum removal	Reference
WO_3-Cu	Dispersion	Xenon lamp with a 420 nm cut-off filter (visible)	Tetracycline / 50 mg L^{-1}	50 mg / 100 mL	96.8% after 60 min	[67]
WO_3/TiO_2	Hydrothermal + calcination	Xenon lamp with a 420 nm cut-off filter (visible)	Methylene blue / 10 mg L^{-1}, metoprolol / 2 mg L^{-1}	50 mg / 50 mL	87.8% and 67.1% after 150 min	[68]
$WO_3/g\text{-}C_3N_4$	Precipitation + calcination	250 W HPMVL lamp (visible)	Carbamazepine, ibuprofen, tartrazine, Rhodamine B / 10 mg L^{-1}	50 mg / 100 mL	78%, 84%, 100%, 100% after 120 min	[69]
Co_3O_4/WO_3	Coprecipitation + dispersion	Mercury lamp with a 420 nm cut-off filter (visible)	Diclofenac sodium / 15 mg L^{-1}	30 mg / 50 mL	90.8% after 180 min	[70]
WO_3/rGO/AgI	Hydrothermal + dispersion	30 W LED lamp (visible)	Amoxicilin / 20 mg L^{-1}	100 mg / 200 mL	86.1% after 240 min	[71]
WO_3/AgBr	Hydrothermal + precipitation	Sunlight (UV–Vis)	Rhodamine B, ofloxacin / 20 mg L^{-1}	50 mg / 200 mL	94.0%, 82.5% after 240 min	[72]
Ag-AgCl/WO_3	Hydrothermal + ultrasonic precipitation	Xenon lamp with a 420 nm cut-off filter (visible)	4-aminobenzoic acid / 10 mg L^{-1}	20 mg / 30 mL	90% after 60 min	[73]
WO_3/AgCl	Hydrothermal	Metal halide lamp (UV–Vis)	Acetaminophen / 5 mg L^{-1}	10 mg / 10 mL	99.6% after 120 min	[22]
WO_3/AgCl	Hydrothermal	Metal halide lamp (UV–Vis)	Acetaminophen / 5 mg L^{-1}	10 mg / 10 mL	100.0% after 30 min	This work

materials, evaluated by the removal of the model contaminant acetaminophen (ACT), was highly influenced by the type of structure-directing agent. The addition of PEG 2000 and Triton X-100 resulted in photocatalytic performance almost similar to that of the material without additive; urea and oxalic acid hindered the removal of ACT, being more evident for the latter; and citric acid led to highly enhanced photocatalytic performance, with 100.0% of acetaminophen removal after 30 min, equivalent to $k = 0.212\ min^{-1}$. The material synthesized with citric acid was further evaluated in scavenging tests, stability tests, in real pharmaceutical effluent and in a continuous micropacked bed reactor. Evaluations of the oxidative species present in the photodegradation reaction showed that $^{\bullet}OH$, $O_2^{\bullet-}$ and h^+ are the main reactive species. Stability tests revealed a reduction in ACT removal capacity of only 18.8% after 4 cycle times. Furthermore, experiments with real effluent showed 83.6% ACT removal after 20 min, while the experiment in continuous mode led to 97.9% of removal in a residence time of 5 min in steady-state operation. These findings provide evidence that the addition of structure-directing agents, especially citric acid, resulted in WO_3-AgCl with enhanced photocatalytic activity for solar driven applications, providing an attractive and cost-efficient alternative for the treatment of real pharmaceutical effluents containing contaminants of emerging concern.

Declaration of competing interest

The authors declare the following financial interests/personal relationships which may be considered as potential competing interests: Priscila Hasse Palharim reports financial support was provided by Coordination of Higher Education Personnel Improvement. Antonio Carlos Silva Costa Teixeira reports financial support was provided by State of Sao Paulo Research Foundation. Antonio Carlos Silva Costa Teixeira reports financial support was provided by National Council for Scientific and Technological Development.

Data availability

Data will be made available on request.

Acknowledgements

The authors express their gratitude to the São Paulo Research Foundation (FAPESP, grants No. 2021/04281-0, 2019/24158-9 and 2018/2171-6), to the National Council for Scientific and Technological Development (CNPq, grants 131467/2017-4 and 311230/2020-2) and to the Coordination for the Improvement of Higher Education Personnel – Brazil (CAPES) – Finance Code 001. In addition, this research used the facilities of the National Nanotechnology Laboratory (LNNano), part of the Brazilian Centre for Research in Energy and Materials (CNPEM), a private non-profit organization under the auspices of the Brazilian Ministry of Science, Technology, and Innovations (MCTI). Naga Vishnu Vardhan Mogili and Ângela Albuquerque Teixeira Neto are acknowledged for the assistance during the experiments (TEM-FEG-20210327, XPS-20220414). Finally, the authors would like to thank Dr. Arnulf Rosspeintner, Dr. Abolfazl Ziarati and M.Sc. Luis Enrique Llanes Montesino, from the Department of Physical Chemistry, University of Geneva, for their valuable contribution with photoluminescence and Mott-Schottky analyses.

Appendix A. Supplementary data

Supplementary data to this article can be found online at https://doi.org/10.1016/j.jphotochem.2023.115433.

References

[1] C. Gómez-Solís, D. Sánchez-Martínez, I. Juárez-Ramírez, A. Martínez-De La Cruz, L. M. Torres-Martínez, Facile synthesis of m-WO_3 powders via precipitation in ethanol solution and evaluation of their photocatalytic activities, J. Photochem. Photobiol. A Chem. 262 (2013) 28–33, https://doi.org/10.1016/j.jphotochem.2013.04.011.

[2] S. Lin, Y. Guo, X. Li, Y. Liu, Glycine acid-assisted green hydrothermal synthesis and controlled growth of WO_3 nanowires, Mater. Lett. 152 (2015) 102–104, https://doi.org/10.1016/j.matlet.2015.03.099.

[3] B. Ma, J. Guo, W.L. Dai, K. Fan, Ag-AgCl/WO_3 hollow sphere with flower-like structure and superior visible photocatalytic activity, Appl Catal B 123–124 (2012) 193–199, https://doi.org/10.1016/j.apcatb.2012.04.029.

[4] P.H. Palharim, B.L.D. dos R. Fusari, B. Ramos, L. Otubo, A.C.S.C. Teixeira, Effect of HCl and HNO_3 on the synthesis of pure and silver-based WO_3 for improved photocatalytic activity under sunlight, J. Photochem. Photobiol. A Chem. 422 (2022) 113550–113562, https://doi.org/10.1016/j.jphotochem.2021.113550.

[5] C.A. Gueymard, The sun's total and spectral irradiance for solar energy applications and solar radiation models, Sol. Energy 76 (2004) 423–453, https://doi.org/10.1016/j.solener.2003.08.039.

[6] M. Fang, X. Tan, Z. Liu, B. Hu, X. Wang, Recent progress on metal-enhanced photocatalysis: a review on the mechanism, Research 2021 (2021) 1–16. doi: 10.34133/2021/9794329.

[7] M. Li, N.H. Shah, P. Zhang, P. Chen, Y. Cui, Y. Jiang, Y. Wang, Mechanism, modification and application of silver-based photocatalysts, Materials Today Sustainability. 22 (2023) 100409–100429, https://doi.org/10.1016/j.mtsust.2023.100409.

[8] W. Wang, Y. Pang, S.N.B. Hodgson, XRD studies of thermally stable mesoporous tungsten oxide synthesised by a templated sol-gel process from tungstic acid precursor, Microporous Mesoporous Mater. 121 (2009) 121–128, https://doi.org/10.1016/j.micromeso.2009.01.014.

[9] P. Chen, H. Fu, S. Yang, K. Lu, Chemical vapor deposition-fabricated manganese-doped and potassium-doped hexagonal tungsten trioxide nanowires with enhanced gas sensing and photocatalytic properties, Nanomaterials 12 (2022) 1208–1221, https://doi.org/10.3390/nano12071208.

[10] L.F. Lopes, F.M. Pontes, L.O. Garcia, D.S.L. Pontes, D. Padovani, A.J. Chiquito, S. R. Teixeira, Y.N. Colmenares, V.R. Mastelaro, E. Longo, Silver-controlled evolution of morphological, structural, and optical properties of three-dimensional hierarchical WO_3 structures synthesized from hydrothermal method, J. Alloy. Compd. 736 (2018) 143–151, https://doi.org/10.1016/j.jallcom.2017.11.095.

[11] B. Ahmed, S. Kumar, A.K. Ojha, P. Donfack, A. Materny, Facile and controlled synthesis of aligned WO3 nanorods and nanosheets as an efficient photocatalyst material, Spectrochim. Acta A Mol. Biomol. Spectrosc. 175 (2017) 250–261, https://doi.org/10.1016/j.saa.2016.11.044.

[12] M. Zych, K. Syrek, M. Pisarek, G.D. Sulka, Synthesis and characterization of anodic WO_3 layers in situ doped with C, N during anodization, Electrochim. Acta 411 (2022) 140061–140071, https://doi.org/10.1016/j.electacta.2022.140061.

[13] X. Wang, H. Zhang, L. Liu, W. Li, P. Cao, Controlled morphologies and growth direction of WO_3 nanostructures hydrothermally synthesized with citric acid, Mater. Lett. 130 (2014) 248–251, https://doi.org/10.1016/j.matlet.2014.05.138.

[14] S.S. Mehta, M.S. Tamboli, I.S. Mulla, S.S. Suryavanshi, Facile hydrothermal synthesis of nanobricks assembled WO_3 microflowers and their ethanol sensing properties, Mater. Lett. 207 (2017) 80–84, https://doi.org/10.1016/j.matlet.2017.07.061.

[15] S.K. Biswas, J.O. Baeg, S.J. Moon, K.J. Kong, W.W. So, Morphologically different WO_3 nanocrystals in photoelectrochemical water oxidation, J. Nanopart. Res. 14 (2012) 667–679, https://doi.org/10.1007/s11051-011-0667-6.

[16] H. Ahmadian, F.S. Tehrani, M. Aliannezhadi, Hydrothermal synthesis and characterization of WO_3 nanostructures: Effects of capping agent and pH, Mater. Res. Express 6 (2019) 105024–105033, https://doi.org/10.1088/2053-1591/ab3826.

[17] D. Sánchez Martínez, A. Martínez-De La Cruz, E., López Cuéllar, Photocatalytic properties of WO_3 nanoparticles obtained by precipitation in presence of urea as complexing agent, Appl. Catal. A 398 (2011) 179–186, https://doi.org/10.1016/j.apcata.2011.03.034.

[18] B. Ajitha, Y.A. Kumar Reddy, P.S. Reddy, H.J. Jeon, C.W. Ahn, Role of capping agents in controlling silver nanoparticles size, antibacterial activity and potential application as optical hydrogen peroxide sensor, RSC, Advances 6 (2016) 36171–36179, https://doi.org/10.1039/c6ra03766f.

[19] C. Suwanchawalit, S. Buddee, S. Wongnawa, Triton X-100 induced cuboid-like $BiVO_4$ microsphere with high photocatalytic performance, J. Environ. Sci. 55 (2017) 257–265, https://doi.org/10.1016/j.jes.2016.04.030.

[20] F. Can, X. Courtois, D. Duprez, Tungsten-based catalysts for environmental applications, Catalysts 11 (2021) 703–781, https://doi.org/10.3390/catal11060703.

[21] N. Taoufik, W. Boumya, M. Achak, M. Sillanpää, N. Barka, Comparative overview of advanced oxidation processes and biological approaches for the removal pharmaceuticals, J. Environ. Manage. 288 (2021) 112404–112426, https://doi.org/10.1016/j.jenvman.2021.112404.

[22] P.H. Palharim, M.C.D. Caira, C. Gusmão, B. Ramos, G.T. dos Santos, O. Rodrigues Jr., A.C.S.C. Teixeira, Effect of temperature and time on the hydrothermal synthesis of WO_3-AgCl photocatalysts regarding photocatalytic activity, Chem. Eng. Res. Des. 188 (2022) 935–953, https://doi.org/10.1016/j.cherd.2022.10.045.

[23] A. Memar, C.M. Phan, M.O. Tade, Controlling particle size and photoelectrochemical properties of nanostructured WO_3 with surfactants, Appl. Surf. Sci. 305 (2014) 760–767, https://doi.org/10.1016/j.apsusc.2014.03.194.

[24] A. Tasaso, P. Ngaotrakanwiwat, Synthesis of nano-WO_3 particles with polyethylene glycol for chromic film, Energy Procedia 79 (2015) 704–709, https://doi.org/10.1016/j.egypro.2015.11.546.

[25] B. Walfort, N. Gartmann, J. Afshani, A. Rosspeintner, H. Hagemann, Effect of excitation wavelength (blue vs near UV) and dopant concentrations on afterglow and fast decay of persistent phosphor SrAl2O4:Eu2+, Dy3+, J. Rare Earths 40 (2022) 1022–1028, https://doi.org/10.1016/j.jre.2021.07.014.

[26] E.H. Sujiono, V. Zharvan, S.A. Poetra, M. Muchtar, A.M. Idris, M.Y. Dahlan, Structure identification of Nd1-xYbxFeO3 (x = 0.01, 0.05 and 0.10) using Rietveld refinement method, Materials Today: Proceedings Journal. 44 (2021) 3381–3384, https://doi.org/10.1016/j.matpr.2020.11.850.

[27] J. Mahía, A. Vieiro, J. Mira, J. Rivas, M.A. López-Quintela, Influence of calcination temperature on lattice parameters and particle size of R2CuO4 compounds (R = Gd, Nd) prepared by a sol-gel method, J. Solid State Chem. 122 (1996) 25–30, https://doi.org/10.1006/jssc.1996.0076.

[28] Y. Ding, C. Zhao, Y. Li, Z. Ma, X. Lv, Effect of calcination temperature on the structure and catalytic performance of the Cu-MCM-41 catalysts for the synthesis of dimethyl carbonate, Quim. Nova 41 (2018) 1156–1161. doi: 10.21577/0100-4042.20170291.

[29] C. Chai, J. Liu, Y. Wang, X. Zhang, D. Duan, C. Fan, Y. Wang, Enhancement in photocatalytic performance of Ag–AgCl decorated with h-WO_3 and mechanism insight, Appl. Phys. A 125 (2019) 96–106, https://doi.org/10.1007/s00339-019-2384-4.

[30] L. Wang, J. Liu, Y. Wang, X. Zhang, D. Duan, C. Fan, Y. Wang, Insight into the enhanced photocatalytic performance of Ag_3PO_4 modified metastable hexagonal WO_3, Colloids Surf A Physicochem Eng Asp 541 (2018) 145–153, https://doi.org/10.1016/j.colsurfa.2018.01.021.

[31] N. Li, T. Chang, H. Gao, X. Gao, L. Ge, Morphology-controlled WO_{3-x} homojunction: hydrothermal synthesis, adsorption properties, and visible-light-driven photocatalytic and chromic properties, Nanotechnology 30 (2019) 415601–415612, https://doi.org/10.1088/1361-6528/ab2a38.

[32] R.A. Senthil, S. Osman, J. Pan, M. Sun, A. Khan, V. Yang, Y. Sun, A facile single-pot synthesis of WO_3/AgCl composite with enhanced photocatalytic and photoelectrochemical performance under visible-light irradiation, Colloids Surf. A 567 (2019) 171–183, https://doi.org/10.1016/j.colsurfa.2019.01.056.

[33] H. Fang, X. Cao, J. Yu, X. Lv, N. Yang, T. Wang, W. Jiang, Preparation of the all-solid-state Z-scheme WO_3/Ag/AgCl film on glass accelerating the photodegradation of pollutants under visible light, J. Mater. Sci. 54 (2019) 286–301, https://doi.org/10.1007/s10853-018-2856-5.

[34] P.R. Jubu, F.K. Yam, V.M. Igba, K.P. Beh, Tauc-plot scale and extrapolation effect on bandgap estimation from UV–vis–NIR data – A case study of β-Ga_2O_3, J. Solid State Chem. 290 (2020) 121576–121584, https://doi.org/10.1016/j.jssc.2020.121576.

[35] P. Makuła, M. Pacia, W. Macyk, How to correctly determine the band gap energy of modified semiconductor photocatalysts based on UV-Vis spectra, J. Phys. Chem. Lett. 9 (2018) 6814–6817, https://doi.org/10.1021/acs.jpclett.8b02892.

[36] J.L. Hammond, N. Bhalla, S.D. Rafiee, P. Estrela, Localized surface plasmon resonance as a biosensing platform for developing countries, Biosensors 4 (2014) 172–188, https://doi.org/10.3390/bios4020172.

[37] H. Jung, I. Yeo, T. Kim, H. Ki, H. Gu, Surface plasmon resonance effect of silver nanoparticles on a TiO_2 electrode for dye-sensitized solar cells, Appl. Surf. Sci. 432 (2018) 266–271, https://doi.org/10.1016/j.apsusc.2017.04.237.

[38] D. Chen, T. Li, Q. Chen, J. Gao, B. Fan, J. Li, X. Li, R. Zhang, J. Sun, L. Gao, Hierarchically plasmonic photocatalysts of Ag/AgCl nanocrystals coupled with single-crystalline WO_3 nanoplates, Nanoscale 4 (2012) 5431–5439, https://doi.org/10.1039/c2nr31030a.

[39] M.S. Alkathy, F.L. Zabotto, K.C.J. Raju, J.A. Eiras, Effect of defects on the band gap and photoluminescence emission of Bi and Li co-substituted barium strontium titanate ceramics, Mater. Chem. Phys. 275 (2022) 125235–125245, https://doi.org/10.1016/j.matchemphys.2021.125235.

[40] V.M. Longo, L.S. Cavalcante, R. Erlo, V.R. Mastelaro, A.T. de Figueiredo, J. R. Sambrano, S. de Lázaro, A.Z. Freitas, L. Gomes, N.D. Vieira, J.A. Varela, E. Longo, Strong violet–blue light photoluminescence emission at room temperature in $SrZrO_3$: Joint experimental and theoretical study, Acta Mater. 56 (2008) 2191–2202, https://doi.org/10.1016/j.actamat.2007.12.059.

[41] M. Petruleviciene, J. Juodkazyte, M. Parvin, A. Tereshchenko, S. Ramanavicius, R. Karpicz, U. Samukaite-Bubniene, A. Ramanavicius, Tuning the photo-luminescence properties of WO_3 layers by the adjustment of layer, Materials. 12 (2020) 2814–2828, https://doi.org/10.3390/ma13122814.

[42] J. Zhang, W. Zhang, Z. Yang, Z. Yu, X. Zhang, T.C. Chang, A. Javey, Vertically aligned tungsten oxide nanorod film with enhanced performance in photoluminescence humidity sensing, Sensors and Actuators, B, Chemical. 202 (2014) 708–713, https://doi.org/10.1016/j.snb.2014.06.009.

[43] N. Getoff, F. Schwörer, V.M. Markovic, K. Sehested, S.O. Nielsen, Pulse radiolysis of oxalic acid and oxalates, J. Phys. Chem. 75 (1971) 749–755, https://doi.org/10.1021/j100676a004.

[44] K. Wenderich, J. Noack, A. Kärgel, A. Trunschke, G. Mul, Effect of temperature and pH on phase transformations in citric acid mediated hydrothermal growth of tungsten oxide, Eur. J. Inorg. Chem. 7 (2018) 917–923, https://doi.org/10.1002/ejic.201701156.

[45] Y. Xu, S. Xu, S. Wang, Y. Zhang, G. Li, Citric acid modulated electrochemical synthesis and photocatalytic behavior of BiOCl nanoplates with exposed 001 facets, Dalton Trans. 43 (2014) 479–485, https://doi.org/10.1039/c3dt52004h.

[46] X. Zhao, X. Zhang, D. Han, L. Niu, Ag supported Z-scheme $WO_{2.9}$/g-C_3N_4 composite photocatalyst for photocatalytic degradation under visible light, Appl. Surf. Sci. 501 (2020) 144258–144267, https://doi.org/10.1016/j.apsusc.2019.144258.

[47] M. Sudha, S. Senthilkumar, R. Hariharan, A. Suganthi, M. Rajarajan, Synthesis, characterization and study of photocatalytic activity of surface modified ZnO nanoparticles by PEG capping, J. Sol-Gel Sci. Technol. 65 (2013) 301–310, https://doi.org/10.1007/s10971-012-2936-y.

[48] Y. Zheng, G. Chen, Y. Yu, Y. Hu, Y. Feng, J. Sun, Urea-assisted synthesis of ultra-thin hexagonal tungsten trioxide photocatalyst sheets, J. Mater. Sci. 50 (2015) 8111–8119, https://doi.org/10.1007/s10853-015-9383-4.

[49] R. Qiao, M. Mao, E. Hu, Y. Zhong, J. Ning, Y. Hu, Facile formation of mesoporous $BiVO_4$/Ag/AgCl heterostructured microspheres with enhanced visible-light photoactivity, Inorg. Chem. 54 (2015) 9033–9039, https://doi.org/10.1021/acs.inorgchem.5b01303.

[50] B. Castanheira, E.R. Triboni, L.D.S. Andrade, F.D.J. Trindade, L. Otubo, A.C.S. C. Teixeira, M.J. Politi, T.B. De Queiroz, S. Brochsztain, Synthesis of novel periodic mesoporous organosilicas containing 1,4,5,8-naphthalenediimides within the pore walls and their reduction to generate wall-embedded free radicals, Langmuir 34 (2018) 8195–8204, https://doi.org/10.1021/acs.langmuir.8b00220.

[51] D.B. Hernández-Uresti, D. Sanchez-Martinez, L.M. Torres-Martinez, Novel visible light-driven $PbMoO_4$/g-C_3N_4 hybrid composite with enhanced photocatalytic performance, J. Photochem. Photobiol. A Chem. 345 (2017) 21–26, https://doi.org/10.1016/j.jphotochem.2017.05.013.

[52] O. Fónagy, E. Szabó-Bárdos, O. Horváth, 1,4-Benzoquinone and 1,4-hydroquinone based determination of electron and superoxide radical formed in heterogeneous photocatalytic systems, J. Photochem. Photobiol., A, Chemistry 407 (2021) 113057–113071, https://doi.org/10.1016/j.jphotochem.2020.113057.

[53] J.T. Schneider, D.S. Firak, R.R. Ribeiro, P. Peralta-Zamora, Use of scavenger agents in heterogeneous photocatalysis: truths, half-truths, and misinterpretations, Phys. Chem. Chem. Phys. 22 (2020) 15723–15733, https://doi.org/10.1039/d0cp02411b.

[54] J.H. Lee, I.N. Tang, Absolute rate constants for the hydroxyl radical reactions with ethane, furan, and thiophene at room temperature, J. Chem. Phys. 77 (1982) 4459–4463, https://doi.org/10.1063/1.444367.

[55] S. Gordon, K.H. Schmidt, E.J. Hart, A pulse radiolysis study of aqueous benzene solutions, J. Phys. Chem. 81 (1977) 104–109, https://doi.org/10.1021/j100517a003.

[56] M. Pelaez, P. Falaras, V. Likodimos, K. O'shea, A.A. de la Cruz, P.S.M. Dunlop, J. A. Byrne, D.D. Dionysiou, Use of selected scavengers for the determination of NF-TiO_2 reactive oxygen species during the degradation of microcystin- LR under visible light irradiation, J. Mol. Catal. A Chem. 15 (2016) 183–189, https://doi.org/10.1016/j.molcata.2016.09.035.

[57] G.V. Buxton, C.L. Greenstock, W.P. Helman, A.B. Ross, Critical review of rate constants for reactions of hydrated electrons, hydrogen atoms and hydroxyl radicals (·OH/·O− in aqueous solution, J. Phys. Chem. Ref. Data 17 (1988) 513–886, https://doi.org/10.1063/1.555805.

[58] O. Al-Madanat, B.N. Nunes, Y. Alsalka, A. Hakki, M. Curti, A.O.T. Patrocinio, D. W. Bahnemann, Application of EPR spectroscopy in TiO_2 and Nb_2O_5 photocatalysis, Catalysts 11 (2021) 1514–1551, https://doi.org/10.3390/catal11121514.

[59] S.S. Kalanur, Structural, optical, band edge and enhanced photoelectrochemical water splitting properties of Tin-doped WO_3, Catalysts 9 (2019) 456–465, https://doi.org/10.3390/catal9050456.

[60] Y. Deng, Y. Zhou, H. Tang, Y. Xu, Y. Tan, H. Zou, Y. Xiang, Synthesis of Z-scheme Bi/TiO_2/WO_3·0.33H_2O heterojunction material for the enhanced photocatalytic degradation of pollutants, J. Mater. Sci. Mater. Electron. 31 (2020) 11276–11285, https://doi.org/10.1007/s10854-020-03676-1.

[61] P. Chatterjee, A.K. Chakraborty, Band-gap engineering of tungsten oxide nanoplates by cobalt ferrite co-catalyst for solar water oxidation, Opt. Mater. 111 (2021) 110610–110617, https://doi.org/10.1016/j.optmat.2020.110610.

[62] A.H.C. Khavar, Z. Khazaee, A. Mahjoub, Electron flux at the Schottky junction of Bi NPs and WO3-supported g-C3N4: an efficient ternary S-scheme catalyst for removal of fluoroquinolone-type antibiotics from water, Environ. Sci. Pollut. Res. Int. 30 (2023) 18461–18479, https://doi.org/10.1007/s11356-022-23370-5.

[63] M.R. Khan, T.W. Chuan, A. Yousuf, M.N.K. Chowdhury, C.K. Cheng, Schottky barrier and surface plasmonic resonance phenomena towards the photocatalytic reaction: Study of their mechanisms to enhance photocatalytic activity, Cat. Sci. Technol. 5 (2015) 2522–2531, https://doi.org/10.1039/c4cy01545b.

[64] X. Yuan, L. Jiang, X. Chen, L. Leng, H. Wang, Z. Wu, T. Xiong, J. Liang, G. Zeng, Highly efficient visible-light-induced photoactivity of Z-scheme Ag_2CO_3/Ag/WO_3 photocatalysts for organic pollutant degradation, Environ. Sci.: Nano. 4 (2017) 2175–2185, https://doi.org/10.1039/C7EN00713B.

[65] G. Li, C. Guo, M. Yan, S. Liu, Cs_xWO_3 nanorods: realization of full-spectrum-responsive photocatalytic activities from UV, visible to near-infrared region, Appl Catal B 183 (2016) 142–148, https://doi.org/10.1016/j.apcatb.2015.10.039.

[66] P. Shandilya, S. Sambyal, R. Sharma, P. Mandyal, B. Fang, Properties, optimized morphologies, and advanced strategies for photocatalytic applications of WO_3 based photocatalysts, J. Hazard. Mater. 428 (2022) 128218–128253, https://doi.org/10.1016/j.jhazmat.2022.128218.

[67] V.T. Quyen, J. Kim, P.-M. Park, P.T. Huong, N.M. Viet, P.Q. Thang, Enhanced the visible light photocatalytic decomposition of antibiotic pollutant in wastewater by using Cu doped WO3, Journal of Environmental, Chem. Eng. 9 (2021) 104737–104744, https://doi.org/10.1016/j.jece.2020.104737.

[68] Q. Wang, W. Zhang, X. Hu, L. Xu, G. Chen, X. Li, Hollow spherical WO_3/TiO_2 heterojunction for enhancing photocatalytic performance in visible-light, Journal

of Water, Process. Eng. 40 (2021) 101943–101953, https://doi.org/10.1016/j.jwpe.2021.101943.

[69] H. Yu, M. Wang, J. Yan, H. Dang, H. Zhu, Y. Liu, M. Wen, G. Li, L. Wu, Complete mineralization of phenolic compounds in visible-light-driven photocatalytic ozonation with single-crystal WO_3 nanosheets: Performance and mechanism investigation, J. Hazard. Mater. 433 (2022) 128811–128828, https://doi.org/10.1016/j.jhazmat.2022.128811.

[70] M.E. Malefane, U. Feleni, A.T. Kuvarega, Cobalt (II/III) oxide and tungsten (VI) oxide p-n heterojunction photocatalyst for photodegradation of diclofenac sodium under visible light, Journal of Environmental, Chem. Eng. 8 (2020) 103560–103576, https://doi.org/10.1016/j.jece.2019.103560.

[71] M.H.T. Tung, T.T.T. Phuong, N.T.P.L. Chi, D.M. The, N.T. Quoc, D.T. Khan, T.-D. Pham, N.V. Khoa, T.T.T. Hien, N.T.D. Cam, Novel amoxicillin degradation via photocatalysis of WO_3/AgI heterojunction decorated on rGO, Ceram. Int. 49 (2023) 10881–10888, https://doi.org/10.1016/j.ceramint.2022.11.281.

[72] J. Piriyanon, P. Takhai, S. Patta, T. Chankhanittha, T. Senasu, S. Nijpanich, S. Juabrum, N. Chanlek, S. Nanan, Performance of sunlight responsive WO_3/AgBr heterojunction photocatalyst toward degradation of Rhodamine B dye and ofloxacin antibiotic, Opt. Mater. 121 (2021) 111573–111590, https://doi.org/10.1016/j.optmat.2021.111573.

[73] Q. Li, G. Duan, J. Luo, X. Liu, Ultrasonic-assisted synthesis of plasmonic Z-scheme Ag/AgCl/WO_3-nanoflakes photocatalyst in geothermal water with enhanced visible-light photocatalytic performance, Journal of Energy, Chemistry 27 (2018) 826–835, https://doi.org/10.1016/j.jechem.2017.05.011.